Institute of Astronomy
Faculty of Mathematics and Physics
Charles University Prague

Astronomical Institute
Academy of Sciences of the Czech republic
Ondřejov

Optical and infrared observations of solid state interplanetary matter

Rostislav Štork

Doctoral thesis

Advisor: Ass. Prof. Dr. Martin Šolc

Consultants: Jaroslav Boček
Dr. Jiří Borovička

September 16, 1998

Acknowledgements

I am very indebted to both of Astronomical Institutes I worked in for excellent conditions for my thesis work. I appreciate the leading of my advisor Ass. Prof. Dr. Martin Šolc and the collaboration with my consultants Dr. Jiří Borovička and Jaroslav Boček.

I want to thank my colleagues Jaroslava Keclíková, Pavel Koten, Dr. Jaroslav Rajchl, Dr. Pavel Spurný for cooperation, their ideas and comments. I commemorate the bright collaboration with Dr. Vladimír Padevět and Prof. Dr. Vladimír Vanýsek, DSc. who left us in the previous years.

I am also indebted to Andrea Budovičová, Dr. Zdeněk Ceplecha, DSc., Hana Ceplechová, Pavel Dostál, Jan Florian, Bruno Jungwiert, Aleš Kolář, Jiljí Mahr, Dr. Pavel Mayer, DSc., Dr. Attila Mészáros, Zdeněk Mrkus, Tomáš Nejezchleba, Jan Němec, Dr. Petr Pecina, Dr. Cyril Polášek, Dr. Petr Pravec, Petr Přidal, Ass. Prof. Dr. Vladimír Karas, Dr. Stanislav Keprta, Lenka Šarounová, Miroslav Šlechta, Michal Varady, Dr. David Vokrouhlický, Radek Vystavěl, Ass. Prof. Dr. Marek Wolf and many others for their interest, comments, ideas and inspiration.

I would like to express my gratitude to my parents for their encouraging support which allow me work in the field of science.

Contents

List of Figures

List of Tables

Chapter 1

Preface

When I finished my work on the Master's thesis I wished to continue research in a related topic. My Master's thesis was based on measurements of space probes to Comet Halley. So I was very happy that I could concentrate on infrared observations of comets based on data from Infrared Space Observatory as the topic of my PhD thesis. I found this work very interesting especially due to possibility to join the big, international project.

I started my PhD studies in October 1993 by improving my background in infrared astronomy and studying theoretical aspects of the problem. But ISO launch was delayed and waiting for observational data made that the subject — IR appearance of dusty comae — came out of the time limits for my PhD Thesis.

So, I gladly accepted an opportunity to work on programme of television observations of meteors — in the group I was before collaborating with. In September 1994 I joined Astronomical Institute, Academy of Science of the Czech Republic in Ondřejov — department of interplanetary matter. I have been working on data processing in TV meteor spectroscopy.

ISO successfully launched on November 17, 1995 and important results have been received till May 16, 1998, when satellite was switched off. But in that time my main work was already TV spectroscopy of faint meteors and I found this topic so exciting that I did not interrupt it when the ISO data begun to be available.

Thus the main method of investigating the meteoroidal matter of cometary origin became the optical spectroscopy of shower meteors accompanied by IR photometry of some comets.

Chapter 2

TV spectroscopy of meteors

2.1 Meteor phenomenon

Fig. 2.1 describes the interaction of interplanetary meteoroidal material with the Earth atmosphere. Four different mechanisms of this phenomenon can be distinguished depending on velocity and mass (Ceplecha, Borovička 1991):

1. "Typical" meteors, that can be seen by naked eye, by television camera or by a telescope, are caused by meteoric bodies (meteoroids) bigger than about 0.01 mm. At heights of about 80–90 km the temperature of the meteoroid surface reaches about 2200 K and meteoroid material starts to sublimate from the surface and fills the surrounding of the body by its hot vapors. After several to few tens of kilometers of flight, meteor terminates its light, because it have lost all of its mass, without decreasing much the velocity.

2. If the dimension of the body exceeds 20 cm (for 15 km/s) there is not enough time for losing all the meteoroid mass. The body slows down to a critical limit of about 3 km/s, when the thermal energy released at the surface of the meteoroid is not sufficient to keep the surface temperature above 2200 K. In this case the meteor, better to say fireball, terminates its light due to small velocity of the meteoroid remnant.

3. If the body is bigger than several meters, its deceleration proceeds slowly and the body hits the Earth's surface before its hypersonic velocity is slowed down. It is a very rare phenomenon and gives rise to an explosive crater.

4. If the dimension of the meteoroid is less than several hundredths of a millimeter, its penetration into the atmosphere cannot be observed as a luminous phenomenon. It is slowed down to less than few kilometers per second already in the outer and extremely rare atmosphere before the meteoroid temperature can reach the evaporation limit. Meteoroid dust particle sediments unchanged and slowly through the atmosphere to the Earth surface.

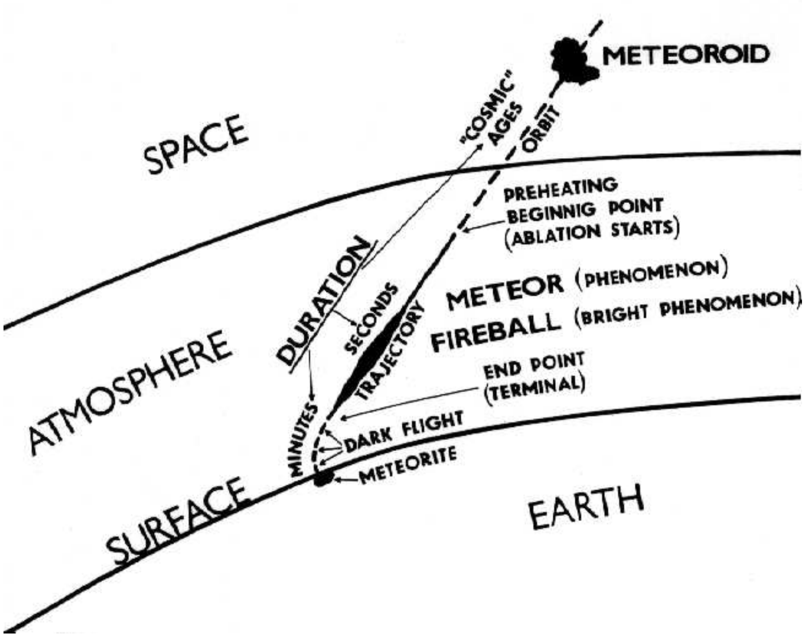

Figure 2.1: Basic terminology of meteors

2.2 TV observation

If we wish to study a faint interplanetary material we have either to make the observations of its scattered and thermal radiation, or to collect samples of it (IDPs and or in situ measurement of probes to Comet Halley), or to record the spectrum of the meteoric light.

In the last case only large bodies (fireballs) can easily be recorded photographically, but fireballs are a phenomenon too rare to be used for statistical comparative studies. This drawback can be eliminated by using a more sensitive television equipment which is capable of recording of large number of spectra of smaller particles than the photography.

Another advantage of the use of television techniques instead of classical photographic method is the good temporal resolution. On the other hand, the spatial resolution is lower.

The TV spectroscopy of meteors was started by the pioneering work of Millman et al. (1971). Further successful observations were performed in Ashchabad (Mukhamednazarov and Maltseva 1989). However, in general, relatively small attention has been devoted to this subject.

Now TV (mainly non-spectroscopic) observations are performed by International Meteor Organization, Nippon Meteor Society, Kyiv University in Ukraine, R. Hawkes' group in Canada.

At the Ondřejov Observatory, regular TV observations of meteor spectra started in 1990, so that the number of registered spectra is large enough for processing by statistical methods.

2.3 Observed interplanetary material

The TV technique can record spectra of meteors brighter than +3 mag. The mass of a particle which cause the +3 mag meteor is about 10^{-6} kg = 0.001 g (Spurný 1991). Such particles originate in cometary nuclei (in the case of shower meteors) and their higher concentration can be expected in coma. However, these particles in coma can be observed only in far infrared spectral range where they emit the thermal radiation, while the scattered light by those particles is lost in the bright shine of the coma dust. The range of ISOPHOT photometry (see Section 7.2) allows however to detect also those larger particles.

2.4 Expected features

Hypotheses about features that we can expect in our TV meteor spectra were listed in several recent papers:

2.4.1 Components in meteor spectra

(Borovička 1994): "Through an analysis of fireball spectra it was found that meteor heads consist of two parts with quite different temperatures. The spectra of both parts can be fitted with a simple thermal equilibrium model. The temperature of the main spectrum is about 4 000 K, and that of the second spectrum is about 10 000 K. There is little evidence for a dependence of temperatures on the meteor velocity. However, the mass and luminosity of the second part relative to the main part grows rapidly with meteor velocity. The high temperature part forms only 0.02 % of the meteor vapor envelope in slow meteors but accounts for more than 5 % in fast meteors. ... This region is very probably related to the meteor shock wave."

Our set of spectra of meteor showers of various velocities allows to study the above mentioned dependence of luminosity of the second spectrum on the meteor velocity.

2.4.2 Unique composition of α Monocerotids

(Jenniskens et al. 1996): "... The double–station observations also provide clues regarding the structure of the dust particles within the α Monocerotid stream. They penetrate deeper into the atmosphere than meteoroids of the Orionid stream (P/Halley) or Perseid stream (P/Swift–Tuttle) and the light curves of the meteors do not show flares."

The Jenniskens' results imply that α Monocerotids are more compact than other showers meteoroids probably due to a lack of volatile elements, and our α Monocerotid spectra seem to be consistent with this hypothesis.

Chapter 3

TV meteor observations in Ondřejov

TV meteor observations started in Ondřejov in 1990. During six years of regular observations tens of meteors and also more than one hundred of meteor spectra were recorded. Recording of meteor spectra is the main part of TV observation programme in the last years.

The first TV observations were prepared and made by Dr. Vladimír Padevět and Jaroslav Boček. Their work were supported by Grant Agency of the Czechoslovak Academy of Sciences, grant no. 30351 — Relation of meteorites to comets (1992–1994; V. Padevět, J. Borovička, J. Boček). Since 1994, after the sudden death of Dr. Padevět, Dr. Borovička became new leader and grant principal investigator. Current team members are:

Dr. Jiří Borovička head, spectra interpretation, software creator

Jaroslav Boček project initiator, experiments creator, observer, technician, image processing

Jaroslava Keclíková searching videotapes for meteors

Rostislav Štork image processing, spectra processing and interpretation

and also non–spectral part of the team:

Dr. Pavel Spurný double station observations

Dr. Jaroslav Rajchl physics of persistent train

Pavel Koten photometry, light curves of meteors

My work was partly routine processing of meteor spectra — scanning digitized images, identification of several bright lines and assigning wavelengths to the spectrum. This work cannot be automatized due to big differences in recorded images. Frequently only part of the spectrum is recorded in the field of view, with various orientations of meteor trajectory and grating, overlapping stars and their spectra, and scanning parameters must be adjusted only after a

camera	nightvision model HT 11–22/SIT (Hiradash Technika — Budapest)
detector	RCA 4804/H SIT–vidicon tube + S 20 photocathode
lens	Meopta-Stigmar f/0.75, f=50 mm
spectral grating	Milton-Roy 300 groves/mm, blazed to 490.0 nm
frame rate	25 frames/s
field of view	15 × 11 degrees
mount	azimuthal
video recorders	S–VHS GRUNDIG GV 280S, S–VHS PANASONIC NV–FS88, bandwidth > 4 MHz
image processor	TESLA VUST
resolution	512 × 512 pixels
dispersion	1.0 nm/pixel in the first order

Table 3.1: Current TV instrumentation at the Ondřejov observatory

thorough inspection. Also recognizing the lines requires human eye and cannot be made automatically by computer. Next step in the data reduction is the use of code written by Dr. Borovička that allows to carry out the spectrum analysis.

3.1 Instrumentation

The principal idea of the TV technique is simple. The TV camera is directed to the sky, a spectral grating mounted on it and recording on video recorder is started.

However, a real situation is a little bit complicated and needs a more expensive equipment. We used a good quality video recorder (at least S–VHS) and very sensitive night vision camera (sensitivity about 10^{-4} lux). Another way, applied mainly by amateur astronomers, is the use of a commercial camcorder and an image intensifier.

Our current instrumentation is summarized in the Table. 3.1 (adapted from (Borovička & Boček 1995)). The limiting magnitude for taking meteor spectrum is about +3 and the time resolution is 0.04 s.

3.2 Image processing

The first step is digitizing of the video record. It produces a sequence of images with a time step of 0.04 s. All images must be dark-frame subtracted and flat-fielded.

Typical image is shown in Fig. 3.1.

The second step is scanning of the spectrum. Scanning path, aperture length, width and angle and scanning step are the optional parameters. We use standard values of the aperture width (2 pixels) and the scanning step (0.5 pixel). The aperture length is set according to the spectrum appearance. We also scan the background level in a spectrum surrounding area. Fig. 3.2 illustrates the scanning process. The background signal is subtracted to obtain

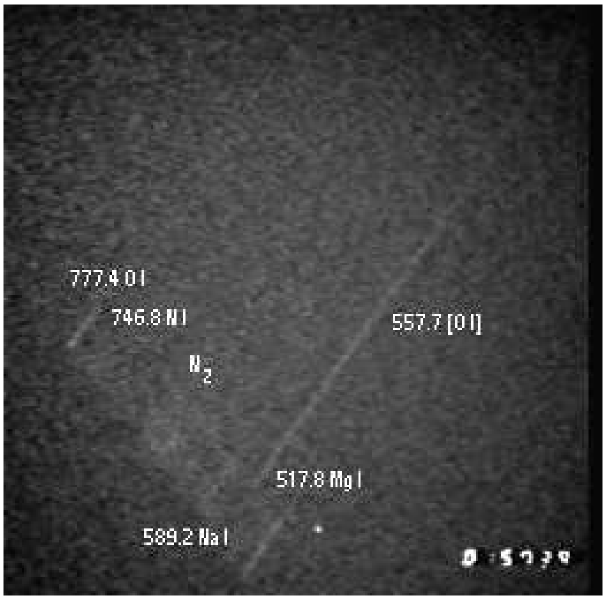

Figure 3.1: Typical digitized image of the meteor spectrum (`S74.74F`)

a purified signal.

Scanning produces a raw spectrum. To set a wavelength scale across the spectrum, it is necessary to find at least one spectral line. If we identify only one line, we suppose that dispersion is 1.05 nm per pixel. In case of more identified spectral lines we can compute the real dispersion.

The spectrum intensities are saved in the equidistant wavelength steps of 0.4 nm. Each intensity means averaged intensity over an interval of 5 pixels. The examples of spectra are shown in Chapter 4.

3.3 Spectral sensitivity

The sensitivity of our detector as a function of wavelength is known. The spectral sensitivity curve was obtained by the observation of spectra of bright standard stars and is shown at Fig. 3.3 (from Borovička & Boček 1995). However, when the spectrum is divided by the spectral sensitivity curve, it produces a noise increase on the spectrum edges and results in an unrealistic 'parabolic' shape of the spectrum. Thus we decided not to calibrate the observed spectrum as a whole.

On the other hand the measured line intensities can be calibrated by using spectral sensitivity at the corresponding wavelengths. So, the spectra in Chapter 4 are not calibrated, but the line intensities in Chapter 5 are.

We divided line intensities by values listed in Table 3.2. The listed sensitivity is normalized to unity at 550 nm.

Several spectra were taken in higher orders. In that case line intensities have been corrected with the knowledge of spectral sensitivity in higher orders.

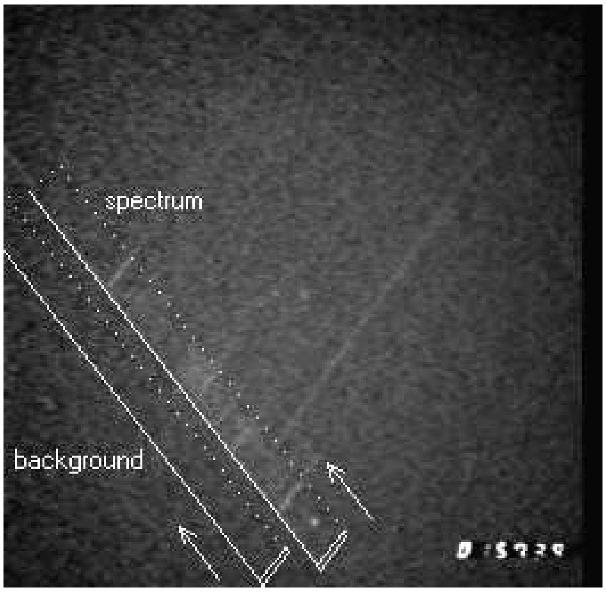

Figure 3.2: Illustration of scanning process

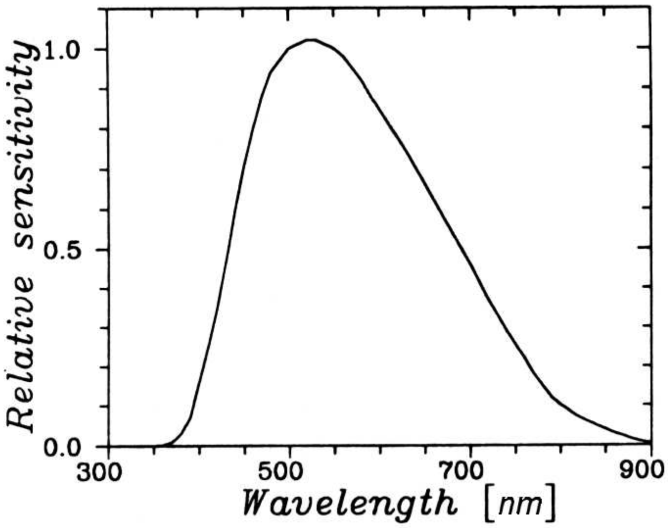

Figure 3.3: The spectral sensitivity curve of our TV system (normalized to unity at 550 nm)

wavelength	line	sensitivity
517.8 nm	Mg I	1.02
557.7 nm	[O I]	0.99
589.2 nm	Na I	0.87
746.8 nm	N I	0.27
777.4 nm	O I	0.15

Table 3.2: Spectral sensitivity at important wavelengths

wavelength	2^{nd} order	3^{rd} order	4^{th} order	-1^{st} order	-2^{nd} order	-3^{rd} order
517.8 nm	0.010	0.0002	0.0005	0.020	0.023	0.028
557.7 nm	0.002	0.0002	0.0006	0.039	0.031	0.030
589.2 nm	0.002	0.0003	0.0007	0.054	0.036	0.031
746.8 nm	0.010	0.0017	0.0012	0.138	0.048	0.033
777.4 nm	0.010	0.0021	0.0014	0.156	0.050	0.034

Table 3.3: Correction factors — sensitivity in various orders

The correction factors (sensitivity/first order sensitivity) are listed in Table 3.3, based on (Borovička 1997). (The spectral grating is blazed to the first order. Remarkable is that the higher orders sensitivity is greater on the non–blazed side then on the blazed one.)

The spectra TVS 01–18 were taken with an experimental spectral grating blazed to the 2^{nd} order and the line intensities have been corrected due to the different parameters of our instrumentation. The correction factors (sensitivity with the old, experimental grating)/(1^{st} order sensitivity with the new grating) are listed in the Table 3.4. Also based on (Borovička 1997).

3.4 Recorded spectra 1990–1994

The results in the following Chapters are based on the evaluation of TV spectra captured during the period 1990–1994. This group is the first one in Ondřejov

wavelength	1^{st} order	2^{nd} order
517.8 nm	0.06	0.56
557.7 nm	0.13	0.42
589.2 nm	0.22	0.29
746.8 nm	1.22	0.20
777.4 nm	1.57	0.18

Table 3.4: The correction factors for the spectra taken with the old, experimental grating

programme which is enough numerous for statistical processing. Also, the α Monocerotids spectra (captured 21/22 XI 1995) were added to this group as a sample of interplanetary material of a distinct composition.

The designations of Ondřejov TV spectra consist of upper case letters "TVS" followed by a sequential number. The spectra TVS 1–78 and added α Monocerotids TVS 156–161 are in our set. Nevertheless, the quality of some faint meteor spectra is bad and a spectrum part with only one line is often recorded. These spectra cannot be used for the comparison of lines intensities and presence.

Thus we selected 44 good quality TV spectra which are usually recorded on several images with a time step of 0.04 s. The time evolution shows significant changes in a meteor spectrum and that is why we prefer to process more images rather then averaging them.

Chapter 4

High quality spectra of cometary meteors

The examples of high quality spectra are shown in this Chapter, but we selected more spectra (all with at least two recognized lines) for further analysis. The list of all selected spectra is given in Section 5.1.

4.1 Perseids

Perseids are the most frequent among our set of spectra, about one half of all. Even if error bars of other showers on Fig. 5.6 are smaller or zero, the points representing the Perseids on Figs. 5.5 and 5.6 are the best defined and other showers can be related to them. The velocity of Perseids is 61 km/s.

4.1.1 TVS 33

TVS 33 is a medium quality spectrum with higher noise due to the Moon light. Fig. 4.1 shows a meteor spectrum on sequence of four images with the time step of 0.04 s. The red edge was not recorded.

The highest peak at 517 nm belongs to Mg I-2 line. Another prominent peak at 589 nm is a sodium line Na I-1. This line is overlapped with atmospheric molecular belt of N_2 (570–600 nm). The second N_2 belt (635–670 nm) is also evident. The last salient feature is a belt on 420–450 nm formed from the group of Fe lines.

4.1.2 TVS 34

TVS 34 is one of our best spectra. Although captured in the moonshine time its signal/noise ratio is very good. Fig. 4.2 shows a sequence of the three best consecutive images.

The blue end is not recorded and the first important feature on the left is the Mg I-2 line (517 nm). The next prominent line is Na I-1 (589 nm) and three fainter lines follows: a group of Fe I-15 (530–550 nm), O I-10 (616 nm), Fe I-168 (650 nm) and atmospheric N I-3 (745 nm). The lines are overlapped

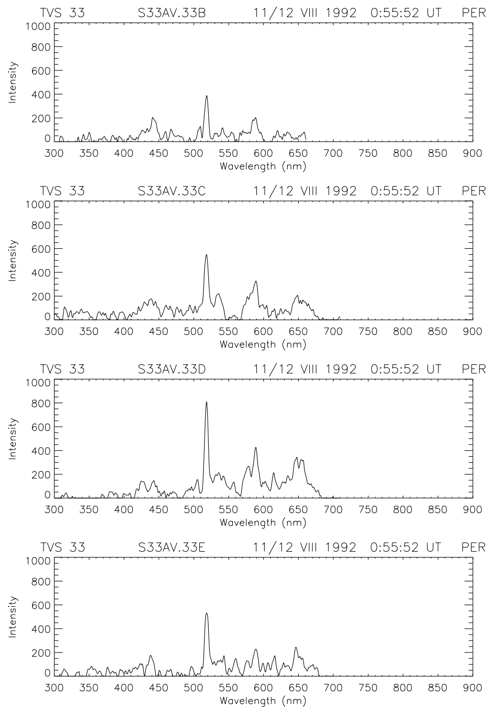

Figure 4.1: Perseid spectrum TVS 33

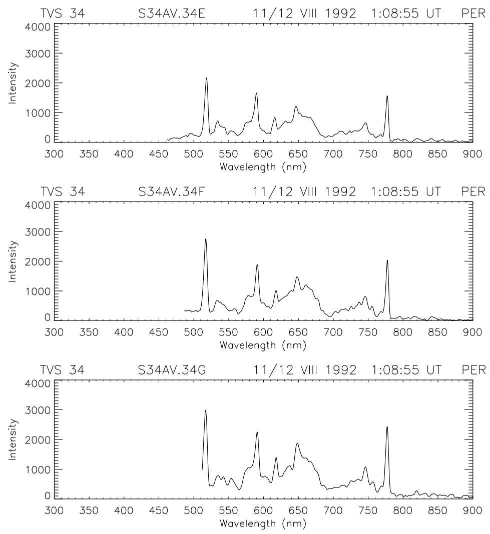

Figure 4.2: Perseid spectrum TVS 34

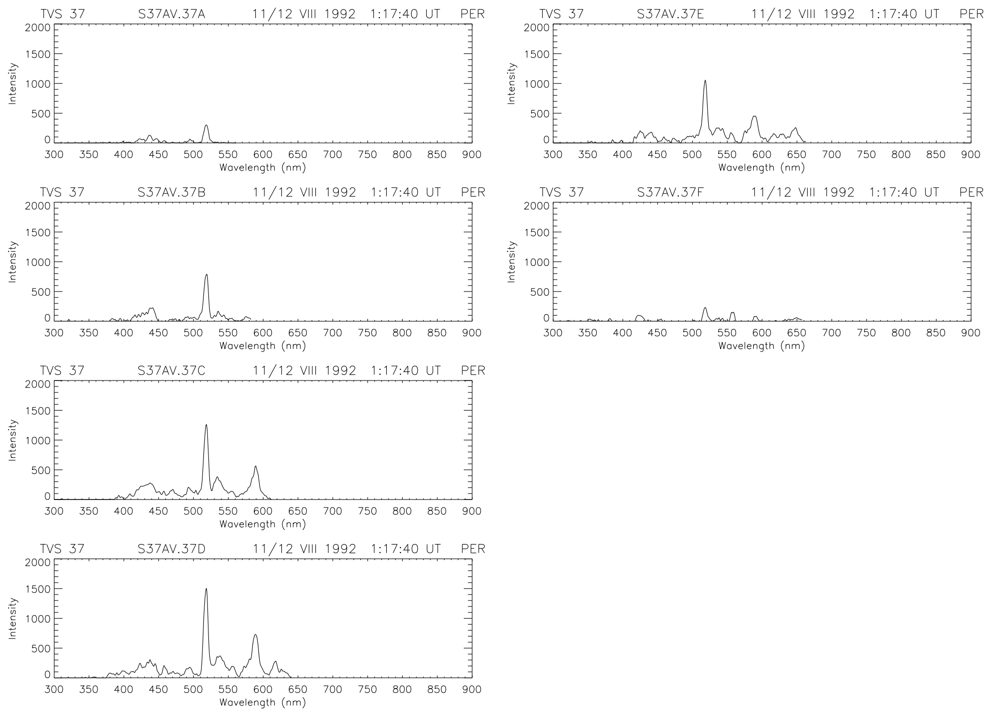

Figure 4.3: Perseid spectrum TVS 37

by three N_2 belts (570–600 nm, 635–670 nm, 730–760 nm). The bright line in the infrared part of the spectrum is O I-1 (777 nm).

4.1.3 TVS 37

TVS 37 illustrates the rapid changes in the meteor spectrum. The time step between images on Fig. 4.3 is 0.04 s, the duration of the entire event was only about 0.2 s.

The recorded spectrum consists of the group of Fe lines (420–450 nm), the brightest line Mg I-2 (517 nm) and the sodium line Na I-1 (589 nm). Also two N_2 belts (570–600 nm, 635–670 nm) can be recognized (`S37AV.37E`).

4.1.4 TVS 67

TVS 67 is a good spectrum but recorded too close to the border of the field of view. Our image processor cannot take a sequence of that spectrum and images must be digitized by the special way which allows to digitalize whole spectrum but don't conserve the value of time step. So, the plots `S67AV.67A-L`[1] show the time evolution with the step of 0.04 s whereas `S67DAV.67A-D` show the whole spectrum, but the time intervals aren't equidistant.

The spectrum features are mostly the same as those in TVS 34. In addition, the forbidden atmospheric line [O I] (558 nm) is recorded. This line appears only

[1]for the explanation of this notation see Section 5.1

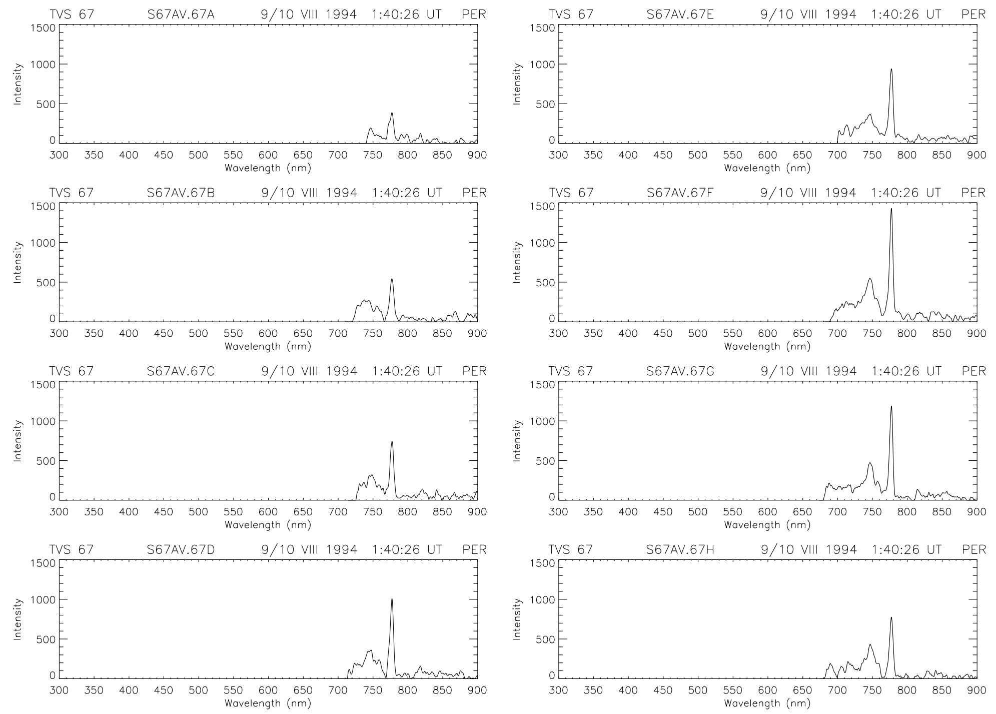

Figure 4.4: Perseid spectrum TVS 67 — part one

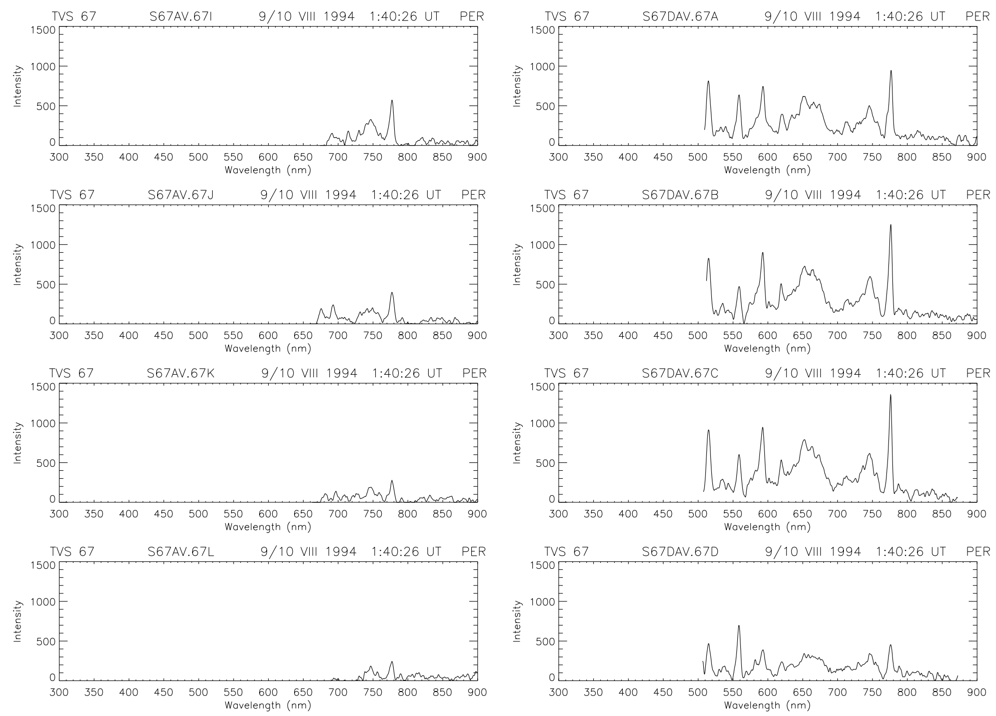

Figure 4.5: Perseid spectrum TVS 67 — part two

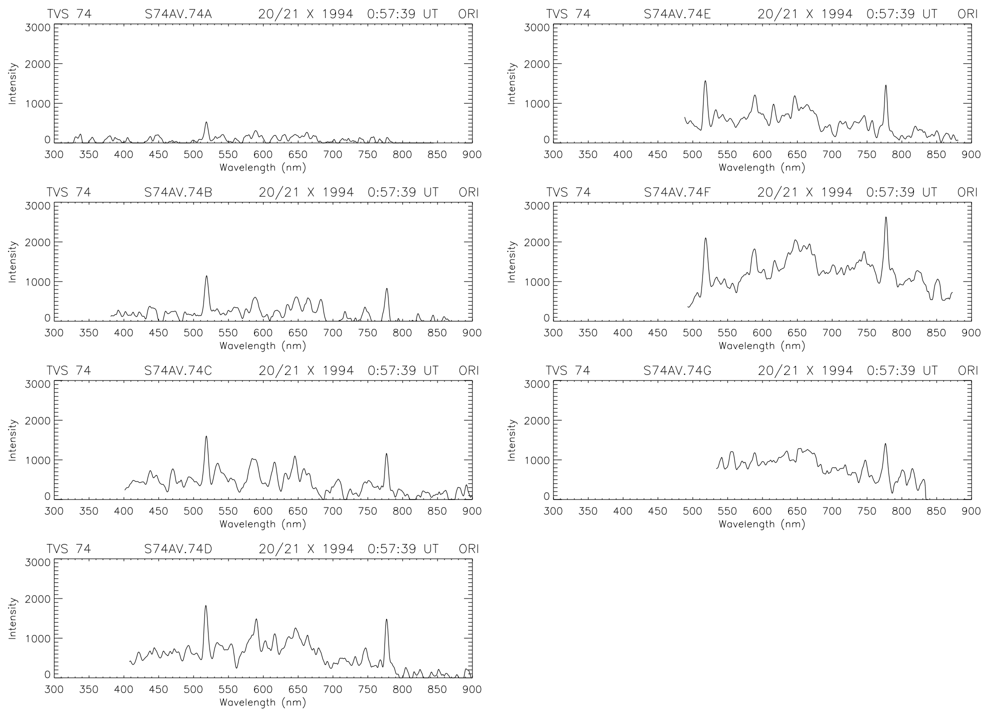

Figure 4.6: Orionid spectrum TVS 74

in faint meteors and its maximum is delayed in time. See S67DAV.67D as an example, when other lines disappear the line [O I] becomes the brightest one.

4.2 Orionids

Orionids' characteristics are similar as Perseids' ones. Their velocity is 67 km/s (Perseids 61 km/s) and both showers come from well known comets. Also our spectra don't show exceptional differences.

4.2.1 TVS 74

TVS 74 is another good illustration of problems with the delayed forbidden line [O I]. As you can see on Fig. 3.1 the [O I] line is very bright. But it isn't featured in spectrum in Fig. 4.6 because the line is out of the scanned area (see Fig. 3.2). . The spectrum on Fig. 4.6 contains all of features described in the previous subsections. It means bright lines Mg I-2 (517 nm), Na I-1 (589 nm) and O I-1 (777 nm), fainter lines O I-10 (616 nm), Fe I-168 (650 nm), N I-3 (745 nm) and three N_2 belts (570–600 nm, 635–670 nm, 730–760 nm) are recorded.

CN bands were also recorded in this spectrum. They are overlapped with N_2 bands in the best images, but in the first images where atmospheric belts are enough faint they can be recognized. In the plot S74AV.74B you can see three belts on approx. 645 nm, 665 nm and 682 nm. The CN bands are significantly

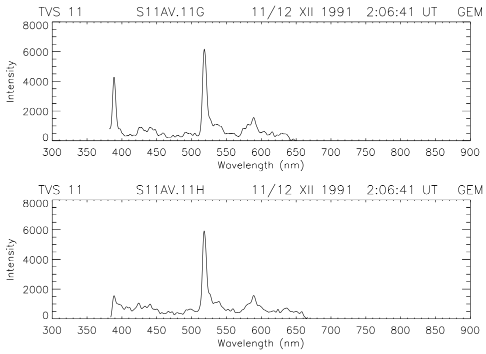

Figure 4.7: Geminid spectrum TVS 11

narrower than those of nitrogen.

4.3 Geminids

Geminids are slow meteors with the velocity of 36 km/s. It means their spectra should show lower intensities of the second spectrum lines (especially O I-1 (777 nm)). In addition the Geminids are known to come from the asteroidal body (3200 Phaeton) that indicates lower amount of volatile elements in these meteoroids.

4.3.1 TVS 11

The part of the second order spectrum together with the red end of the first order spectrum are recorded on TVS 11. The line on the left in Fig. 4.7 is the first order infrared line O I-1 (777 nm), displayed on 389 nm in the second order plot. The brightest line is Mg I-2 (517 nm). The Na I-1 (589 nm) is faint here, overlapped by N_2 belt (570–600 nm). A broad peak 425–450 nm is supposed to be a group of Fe lines together with a wake radiation.

4.3.2 TVS 17

TVS 17 is a faint spectrum but thanks to the dark night without Moon the features are clear. Fig. 4.8 shows lines Mg I-2 (517 nm), Na I-1 (589 nm), O I-1 (777 nm) and the main N_2 belt 635–670 nm.

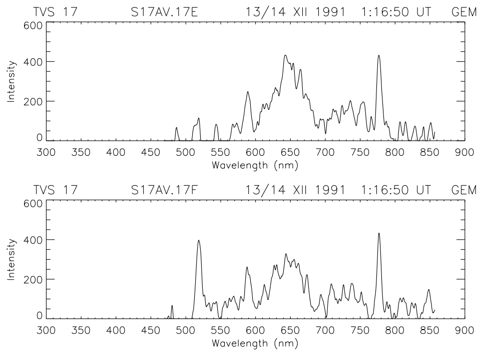

Figure 4.8: Geminid spectrum TVS 17

4.4 Quadrantids

Quadrantids are represented by only one point in Fig. 5.5 and we cannot make any conclusions about the entire shower. Nevertheless, our Quadrantid spectrum corresponds with linear dependencies on Figs. 5.5 and 5.6. The velocity of Quadrantids is 42 km/s.

4.4.1 TVS 65

TVS 65 is our best spectrum supposed to belong to a Quadrantid. The time sequence cannot be taken, there are only two single scanned images on Fig. 4.9. The bright lines are Mg I-2 (517 nm) and O I-1 (777 nm), also N_2 belt 635–670 nm is noticeable.

4.5 δ Aquarids

δ Aquarids is another less populated shower in our set. Likewise Quadrantids the recorded δ Aquarids also can't give reliable results but they follow the general dependencies. The velocity of δ Aquarids is 44 km/s.

4.5.1 TVS 42

TVS 42 is very good spectrum but the time sequence cannot be extracted from the records in that case too. So, the time moments on Fig. 4.10 are taken

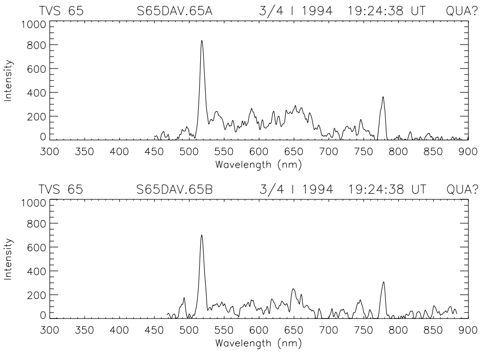

Figure 4.9: Quadrantid spectrum TVS 65

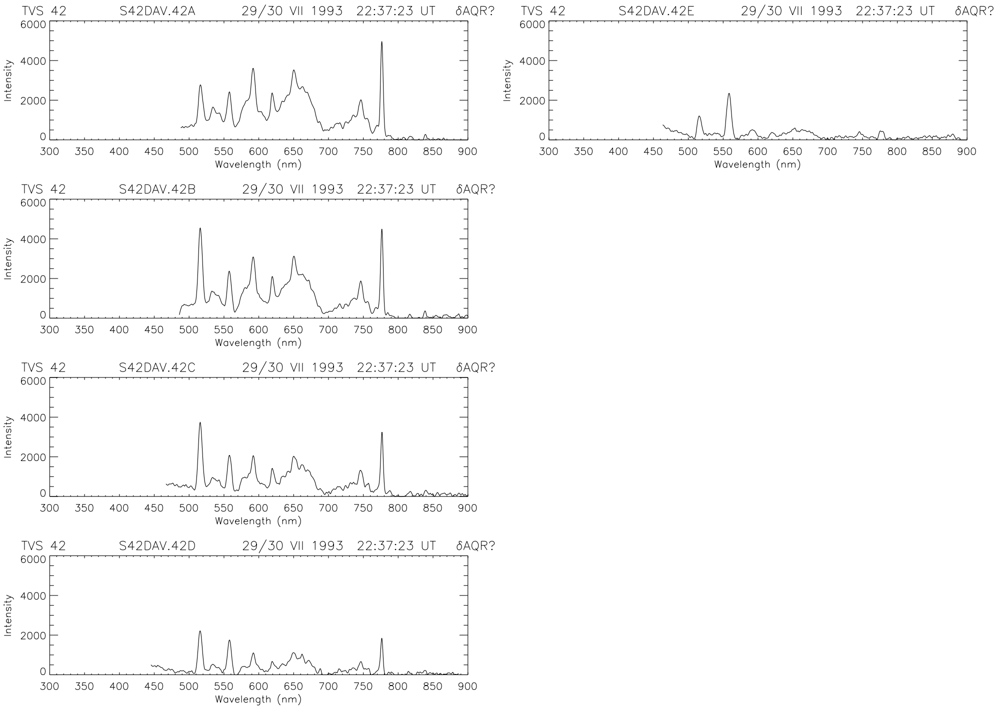

Figure 4.10: δ Aquarid spectrum TVS 42

with a non equidistant step.

There are all lines mentioned in previous subsections in this spectrum: Mg I-2 (517 nm), [O I] (558 nm), Na I-1 (589 nm), O I-10 (616 nm), Fe I-168 (650 nm), N I-3 (745 nm), O I-1 (777 nm). Also three atmospheric N_2 belts (570–600 nm, 635–670 nm, 730–760 nm) are recorded.

Note that the brightness of [O I] increases when all other lines disappear.

4.6 α Monocerotids

Although the aim of our work is a complete processing of collection 1990–1994 of Ondřejov TV meteor spectra we decided to add spectra from November 22, 1995 to our set. During that night α Monocerotids outburst was observed and several, at least four spectra were taken; in other cases the identification is not sure.

We suppose that α Monocerotids have lower amount of volatile elements (Section 2.4.2) and so our spectra represent a sample of interplanetary material with a specific composition. They also bring new entries into a statistics in Chapter 5.

The velocity of α Monocerotids is 64 km/s but their spectra look unlike Perseids (61 km/s) and Orionids (67 km/s). The hypothesis concerning low amount of volatile elements (Section 2.4.2) is confirmed. The sodium line Na I-1 (589 nm) is very faint in all α Monocerotid spectra.

4.6.1 TVS 161

TVS 161 is our brightest α Monocerotid spectrum taken during the 1995 outburst. The prominent lines on Fig. 4.11 are Mg I-2 (517 nm) and O I-1 (777 nm). Although the N_2 belts (570–600 nm, 635–670 nm, 730–760 nm) and the faint lines O I-10 (616 nm), Fe I-168 (650 nm), N I-3 (745 nm) are visible the intensity of Na I-1 (589 nm) is very low.

4.7 Unknown, sporadic meteors

It is hard to say anything about sporadic meteors generally. Their origin, composition and velocity is different, of course.

Selected TVS 13 and TVS 43 are examples of some interesting cases. TVS 13 is one of our old spectra taken with the previous, old grating. TVS 43 is our only one record of a stationary meteor.

4.7.1 TVS 13

TVS 13 on Fig. 4.12 shows a difference of old spectra taken with another grating. The technique with old, experimental grating was more sensitive in the red and infrared ranges. Note the recorded noise is highest in the above mentioned infrared range. Also, the O I-1 (777 nm) is significantly brighter than Mg I-2 (517 nm).

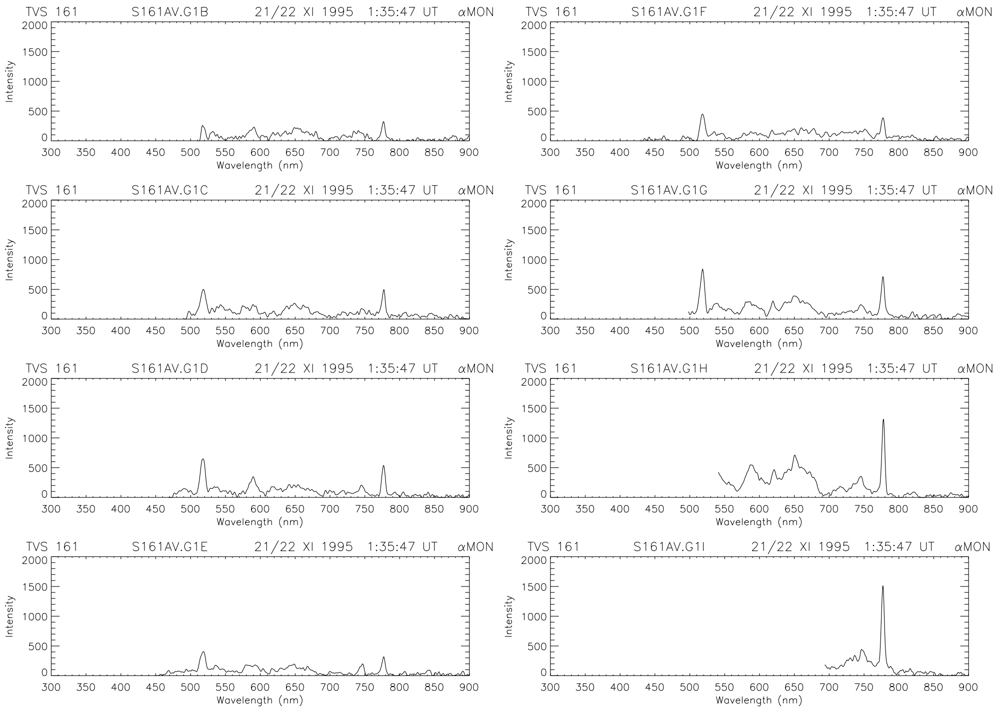

Figure 4.11: α Monocerotid spectrum TVS 161

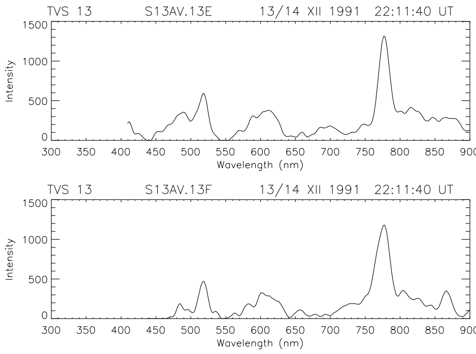

Figure 4.12: Meteor spectrum TVS 13

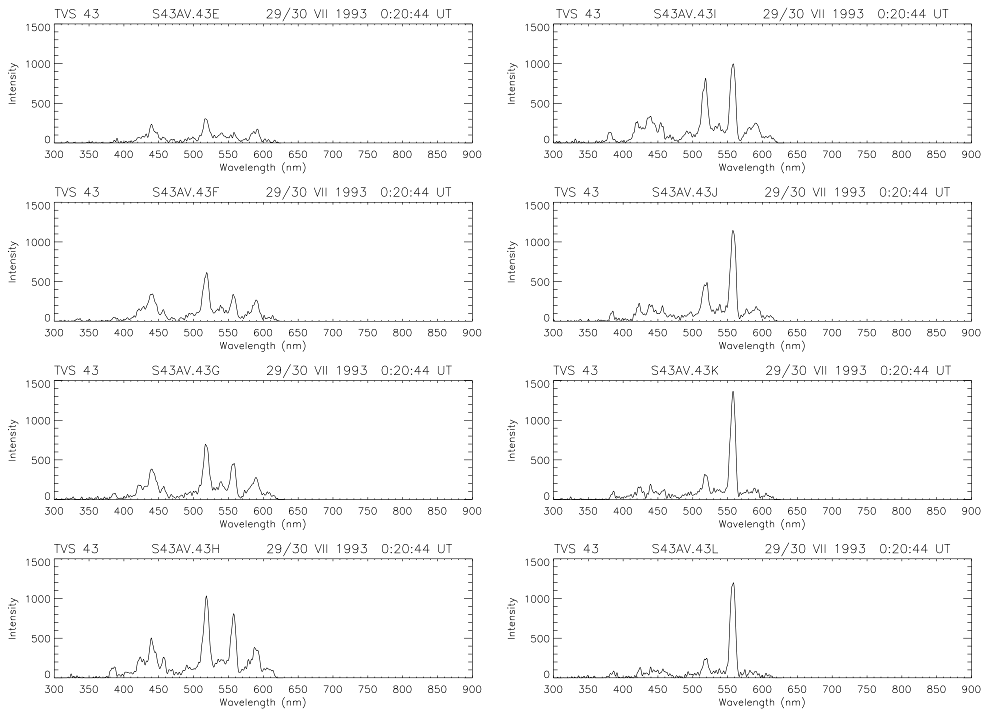

Figure 4.13: Meteor spectrum TVS 43

4.7.2 TVS 43

TVS 43 is a unique spectrum of a stationary meteor. There is no problem with the delayed [O I] line because lines are recorded as points in the row. Thus Fig. 4.13 is the best example showing the delay of forbidden line [O I] (558 nm).

Other recorded features are Mg I-2 (517 nm), Na I-1 (589 nm) and Fe group (420–450 nm).

4.8 Very slow meteor TVS 73

The duration of TV meteors is usually several tenths of second. TVS 73 represent the only exception in our set of Ondřejov TV spectra. We have recorded 30 images with the step of 0.04 s. Our field of view is 10×10 degrees, so the angular velocity was about 10 degrees per second. Elevation was about 45°. Assuming the height was about 80 km we can estimate the lower limit of the meteor velocity. It is about 20 km/s.

The Figures 4.14, 4.15, 4.16 and 4.17 show the slow evolution of the spectrum. Typical features of this slow meteor spectrum are the high ratio of mineral over atmospheric lines (main spectrum over second one) and also high Na/Mg ratio probably caused by higher excitation potential of Mg I-2.

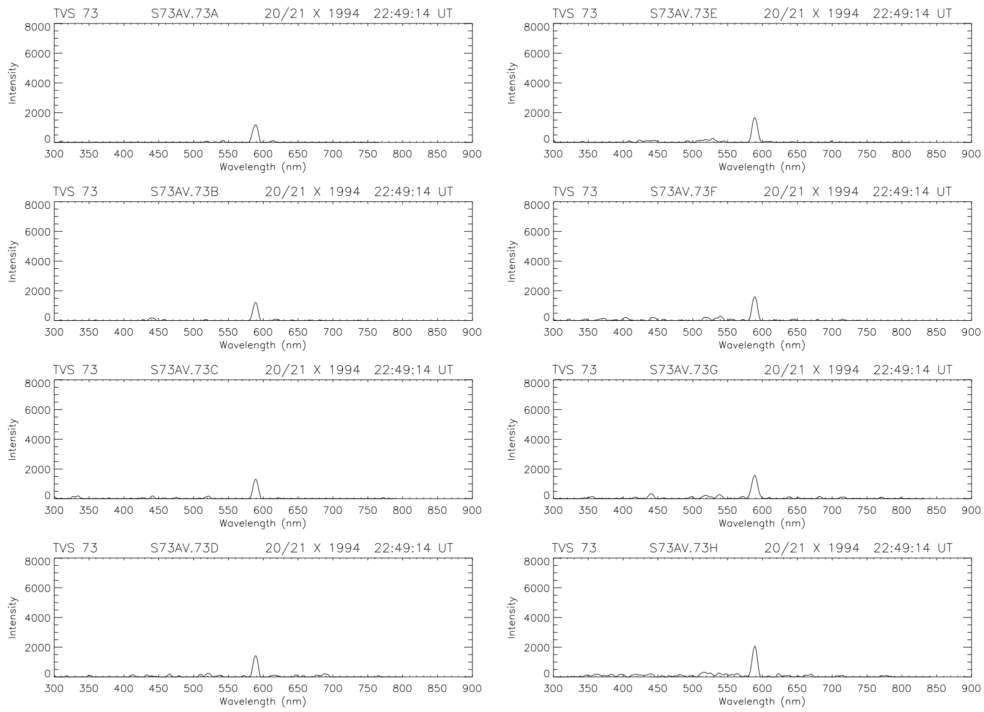

Figure 4.14: Spectrum of the very slow meteor TVS 73 — part one

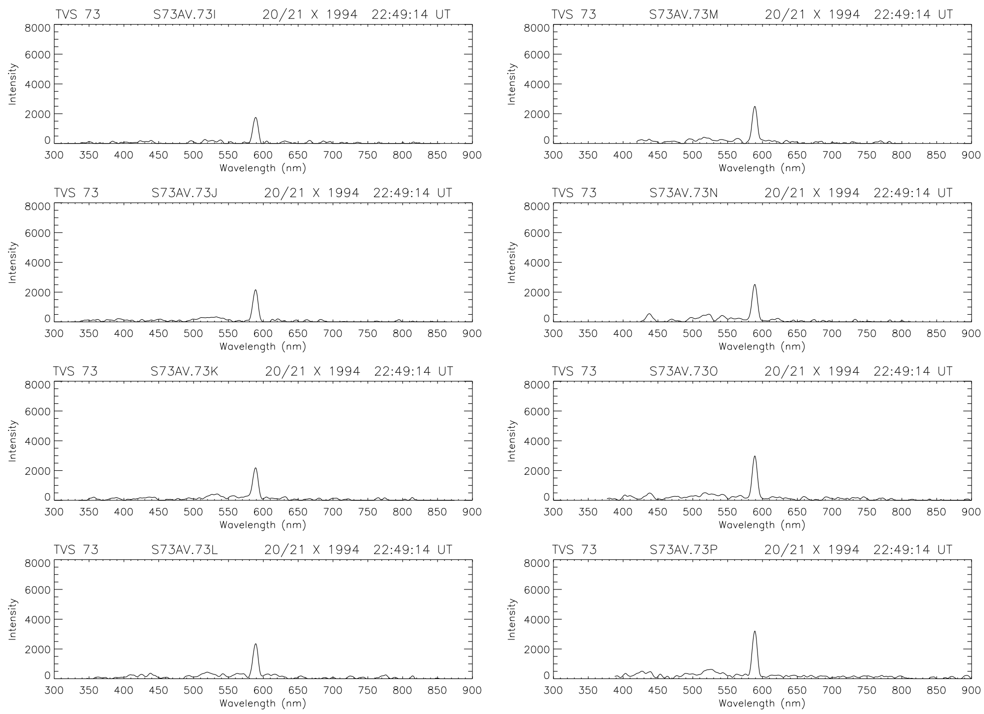

Figure 4.15: Spectrum of the very slow meteor TVS 73 — part two

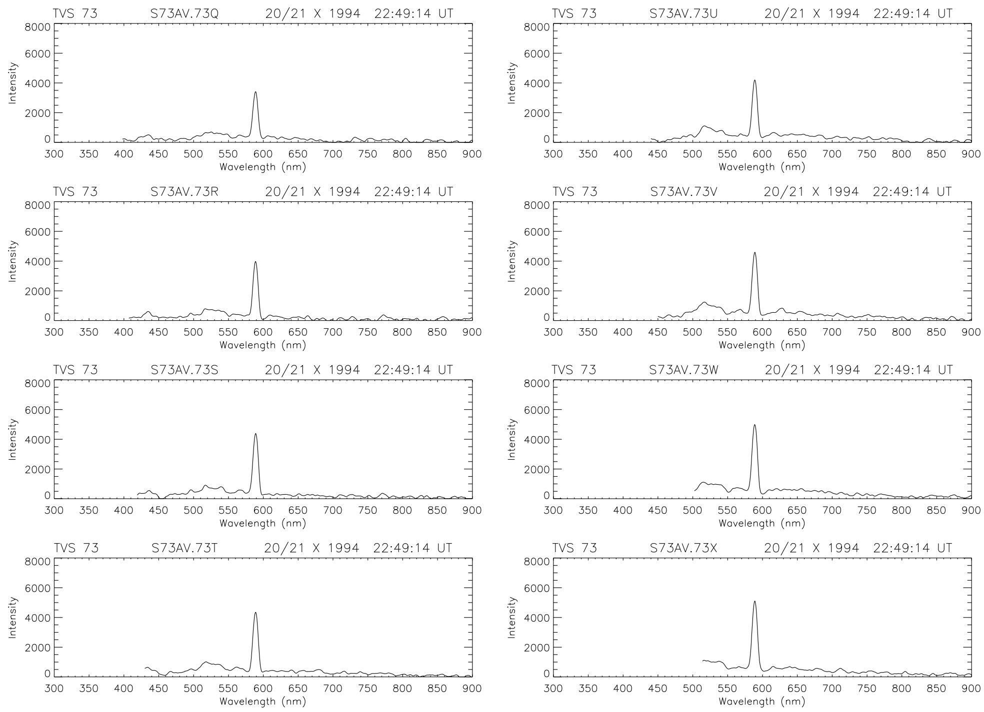

Figure 4.16: Spectrum of the very slow meteor TVS 73 — part three

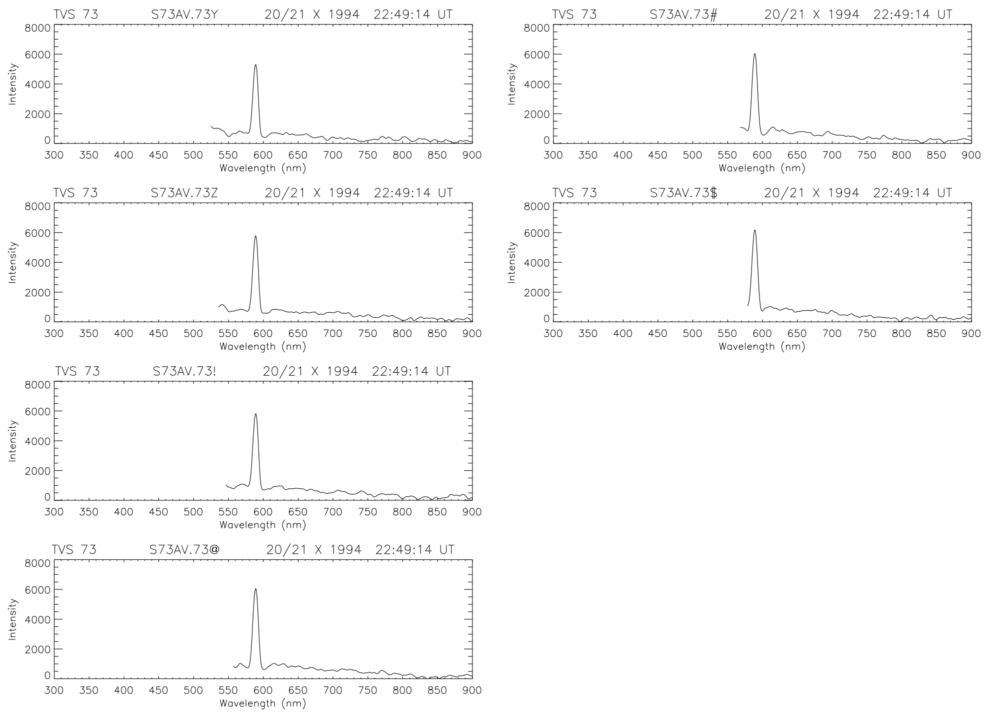

Figure 4.17: Spectrum of the very slow meteor TVS 73 — part four

Chapter 5

Statistically significant differences in observed spectra

5.1 Set of studied spectra

As mentioned in the Section 3.4 we choose 44 good quality spectra with several images of each. The designation of an image is for example `S42AV.42C`, where the last letter indicates the sequence order. `AV` means 'averaged', every spectrum point is average of the small (5 pixels) interval in a raw spectrum.

If '`D`' appears in an image name, the spectrum is recorded too close to the edge of the field of view and must be digitized by the special way.

For statistical processing we used spectra recorded on the following images:

Perseids

```
S05AV.05B  S05AV.05C  S05AV.05D  S05AV.05E
S26AV.26G  S26AV.26H
S29AV.29E  S29AV.29F  S29AV.29G  S29AV.29H  S29AV.29I  S29AV.29J  S29DAV.29F
S30AV.30B  S30AV.30C  S30DAV.30B
S33AV.33B  S33AV.33C  S33AV.33D  S33AV.33E
S34AV.34E  S34AV.34F  S34AV.34G
S37AV.37A  S37AV.37B  S37AV.37C  S37AV.37D  S37AV.37E  S37AV.37F
S47AV.47A  S47AV.47B  S47AV.47C
S48AV.48B  S48AV.48C  S48AV.48D  S48AV.48E
S52AV.52C  S52AV.52D  S52AV.52E  S52DAV.52A
S54DAV.54A S54DAV.54B S54DAV.54C S54DAV.54D
S56AV.56B  S56AV.56C  S56AV.56D  S56AV.56E  S56AV.56F
S57AV.57F  S57AV.57G  S57AV.57H  S57AV.57I
S67AV.67A  S67AV.67B  S67AV.67C  S67AV.67D  S67AV.67E  S67AV.67F  S67AV.67G  S67AV.67H
S67AV.67I  S67AV.67J  S67AV.67K  S67AV.67L  S67DAV.67A S67DAV.67B S67DAV.67C S67DAV.67D
S71AV.71C  S71AV.71D  S71AV.71E  S71AV.71F  S71AV.71G  S71AV.71H  S71AV.71I  S71AV.71J
S53AV.53D  S53AV.53E  S53AV.53F
```

Orionids

```
S03DAV.03A S03DAV.03B S03DAV.03C S03DAV.03D
S74AV.74A  S74AV.74B  S74AV.74C  S74AV.74D  S74AV.74E  S74AV.74F  S74AV.74G
S75DAV.75A S75DAV.75B
S76AV.76D  S76AV.76E
S78AV.78B  S78AV.78C  S78AV.78D
```

Geminids

```
S11AV.11G  S11AV.11H
S16AV.16F  S16AV.16G  S16AV.16H  S16AV.16I  S16AV.16J  S16AV.16K  S16AV.16L  S16AV.16M
S16AV.16N
S17AV.17E  S17AV.17F
S10AV.10C  S10AV.10D  S10AV.10E  S10AV.10F  S10AV.10G
```

Quadrantids

```
S65DAV.65A S65DAV.65B
```

δ Aquarids

```
S21AV.21C  S21AV.21D  S21AV.21E  S21AV.21F
S42DAV.42A S42DAV.42B S42DAV.42C S42DAV.42D S42DAV.42E
```

α Monocerotids

```
S156AV.F6A S156AV.F6B
S158AV.F8A S158AV.F8B S158AV.F8C S158AV.F8D
S159AV.F9A S159AV.F9B S159AV.F9C S159AV.F9D S159AV.F9E S159AV.F9F
S161AV.G1B S161AV.G1C S161AV.G1D S161AV.G1E S161AV.G1F S161AV.G1G S161AV.G1H S161AV.G1I
```

unknown, sporadic

```
S13AV.13E  S13AV.13F
S22DAV.22A
S23DAV.23A S23DAV.23B
S27AV.27E  S27AV.27F
S43AV.43E  S43AV.43F  S43AV.43G  S43AV.43H  S43AV.43I  S43AV.43J  S43AV.43K  S43AV.43L
S44AV.44B  S44AV.44C  S44AV.44D  S44AV.44E  S44AV.44F  S44AV.44G  S44AV.44H  S44AV.44I
S44DAV.44A
S72AV.72E  S72AV.72F  S72AV.72G  S72AV.72H
S24AV.24D  S24AV.24E  S24AV.24F  S24AV.24G
```

very slow meteor TVS 73

```
S73AV.73A  S73AV.73B  S73AV.73C  S73AV.73D  S73AV.73E  S73AV.73F  S73AV.73G  S73AV.73H
S73AV.73I  S73AV.73J  S73AV.73K  S73AV.73L  S73AV.73M  S73AV.73N  S73AV.73O  S73AV.73P
S73AV.73Q  S73AV.73R  S73AV.73S  S73AV.73T  S73AV.73U  S73AV.73V  S73AV.73W  S73AV.73X
S73AV.73Y  S73AV.73Z  S73AV.73!  S73AV.73@  S73AV.73#  S73AV.73$
```

5.2 Intensity plots

The spectra of which examples are shown in Chapter 4 contain several lines. However only four lines were found to be enough bright in the significant number of recorded spectra and can be used for statistical processing.

We measured spectrum intensity at wavelengths 517.8 nm (Mg I), 589.2 nm (Na I), 746.8 nm (N I) and 777.4 nm (O I). The intensity is produced by scanning pixel intensities of the recorded image and is given in the relative units only.

The measured values were calibrated by spectral sensitivity curve of our technique (see Section 3.3).

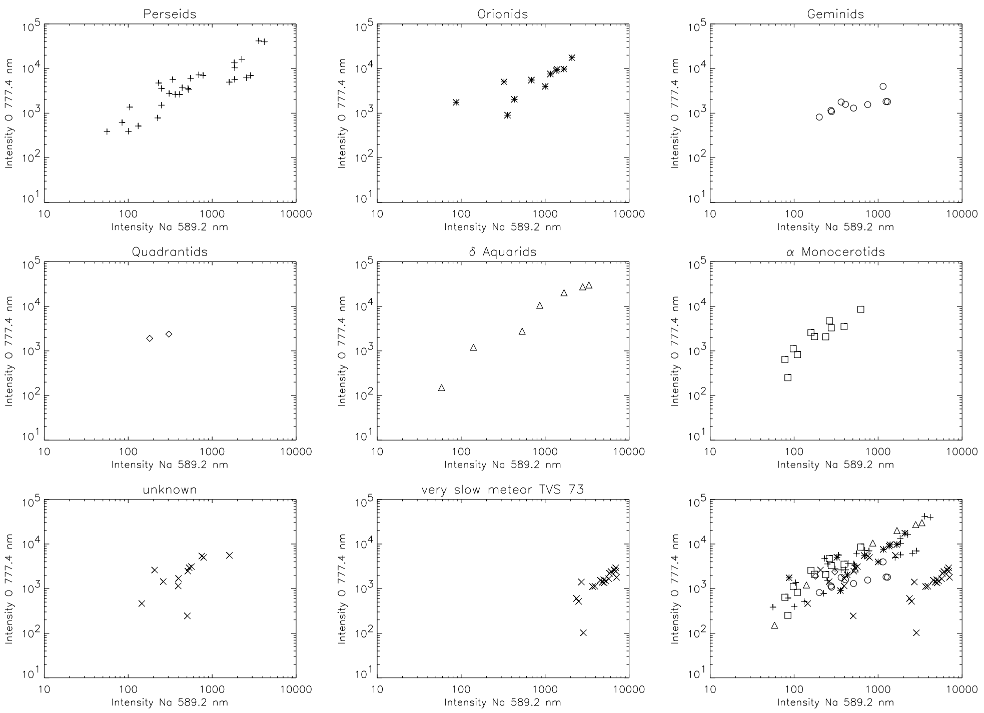

Figure 5.1: Na and O intensities in the studied spectra

5.2.1 Na and O intensities

The points on Fig. 5.1 fall on one line because the meteor spectra show the correlation of intensities of Na and O lines. However, some differences between showers are apparent.

The O I-1 line is fainter in spectra of slower meteors (Geminids and very slow meteor TVS 73). It's probably caused by a strong dependence of the brightness of the second spectrum (which O I-1 belongs to) on the meteor velocity (see Section 2.4.1).

On the other hand, α Monocerotids have lower amount of sodium and so the corresponding points on Fig. 5.1 are shifted to the left.

5.2.2 Mg and O intensities

Plots on Fig. 5.2 show linear dependence in individual showers, but they differ in the line slope.

As mentioned in the previous subsection the amount of the second spectrum is lower in slow meteors. That is why the Geminids plots are shifted to the right and down. The shift of another slow meteor TVS 73 isn't so clear because both of Mg and O lines are very faint and affected by noise.

The high spread in left lower part of the diagram is caused by worse signal/noise ratio in the case of faint meteors.

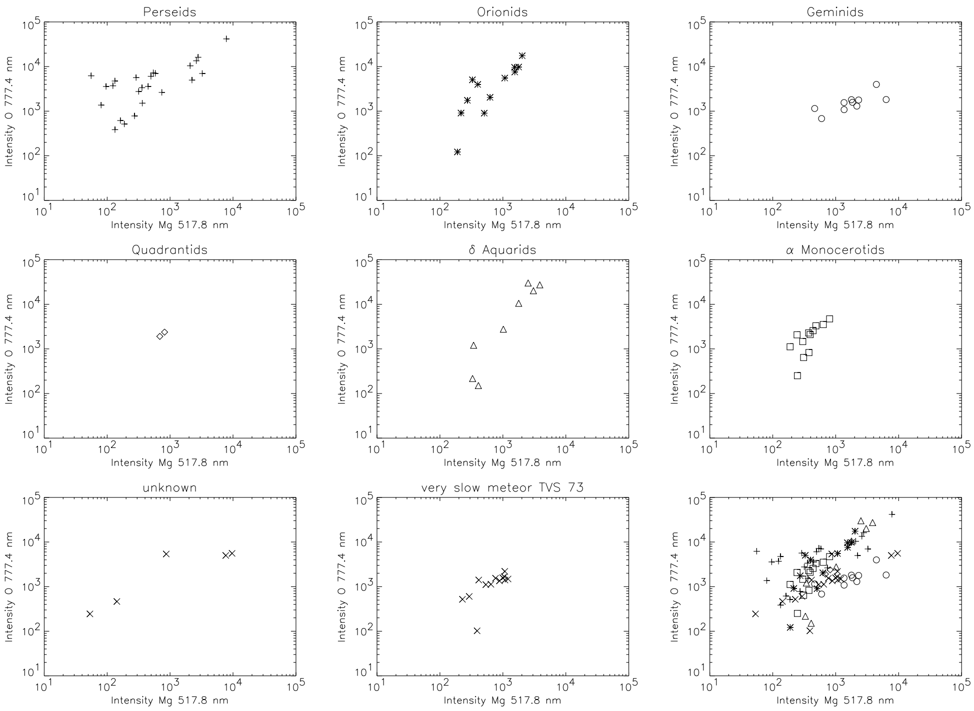

Figure 5.2: Mg and O intensities in the studied spectra

5.2.3 Mg and Na intensities

The most important features of Fig. 5.3 are:

- The Geminid points are shifted to the right. Geminids are known to have lower amount of volatile elements because they originate from asteroid [(3200) Phaeton].
- The Mg I-2 intensity is low in the slow meteor spectrum TVS 73. It may be caused by higher excitation potential of this line (Mg I-2 2.72 eV, Na I-1 0.00 eV[1]). In case of higher velocities, both lines are saturated and optically thick and this phenomenon isn't important.

5.2.4 O and N intensities

The O I-1 and N I-1 lines are both atmospheric and both belong to the second spectrum. So the correlation between those lines is the strongest one of all plotted combinations and the points on Fig. 5.4 represent an almost perfect line.

5.3 Selected images

All good quality images were used for the previous plots (Figs. 5.1, 5.2, 5.3 and 5.4) and a spectrum is represented by several points of the corresponding

[1] <0.005 eV

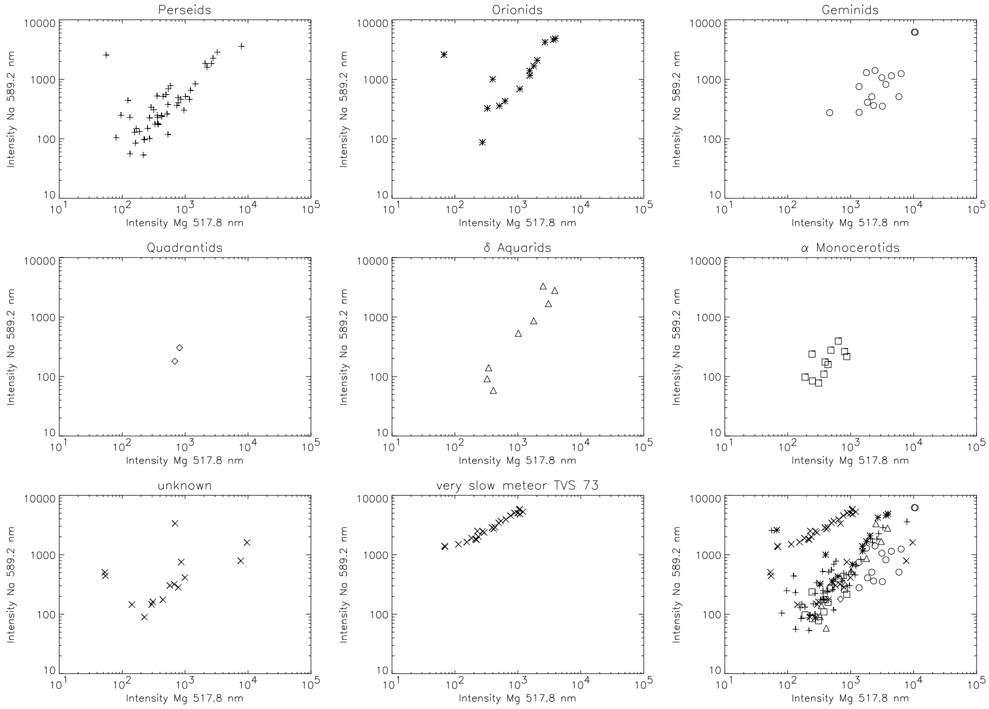

Figure 5.3: Mg and Na intensities in the studied spectra

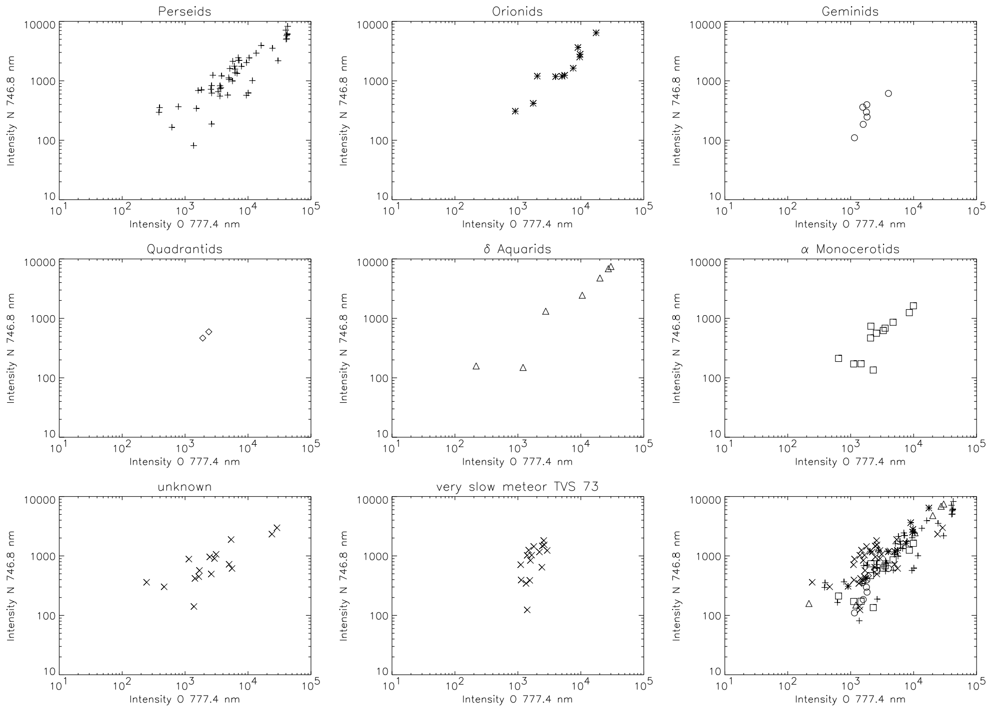

Figure 5.4: O and N intensities in the studied spectra

time steps. For further analysis we selected the best image of each spectrum. The use of selected images in the previous plots doesn't give good results. The points in the lower left part of the diagrams disappear because they represent fainter intensities in the first or final time steps.

Nevertheless we can use the selected images for estimating the ratios of line intensities. The most interesting plot is the velocity dependence of those ratios.

The list of selected images follows:

Perseids

`S05AV.05D S26AV.26G S29DAV.29F S30DAV.30B S33AV.33D S34AV.34G S37AV.37D S47AV.47A`
`S48AV.48C S52AV.52D S54DAV.54A S56AV.56E S57AV.57F S67DAV.67C S71AV.71E S53AV.53E`

Orionids

`S03DAV.03B S74AV.74F S75DAV.75B S76AV.76D S78AV.78C`

Geminids

`S11AV.11G S16AV.16F S17AV.17F S10AV.10E`

Quadrantids

`S65DAV.65A`

δ Aquarids

`S21AV.21E S42DAV.42B`

α Monocerotids

`S156AV.F6A S159AV.F9B S161AV.G1G`

very slow meteor TVS 73

`S73AV.73V`

Of course, sporadic meteors were not included in plots on Figs. 5.5 and 5.6 because the velocity is known only for shower meteors. Only in the case of the extraordinary slow meteor TVS 73 we estimated its velocity (see Section 4.8).

5.4 Dependence on velocity

Figs. 5.5 and 5.6 show the similar plots. The use of weighted[2] averages with standard deviation bars (Fig. 5.6) would be correct but it will not show how many spectra were averaged and how significant shower value is. Thus I find Fig. 5.5 to demonstrate better the dependence.

The Na/O ratio decreases with increasing velocity. All showers are in compliance with this relation except α Monocerotids. The differences in α Monocerotids spectra aren't caused by velocity and so they indicate rather differences in the meteoroidal composition.

[2]the weight is the intensity of lines — meteor brightness

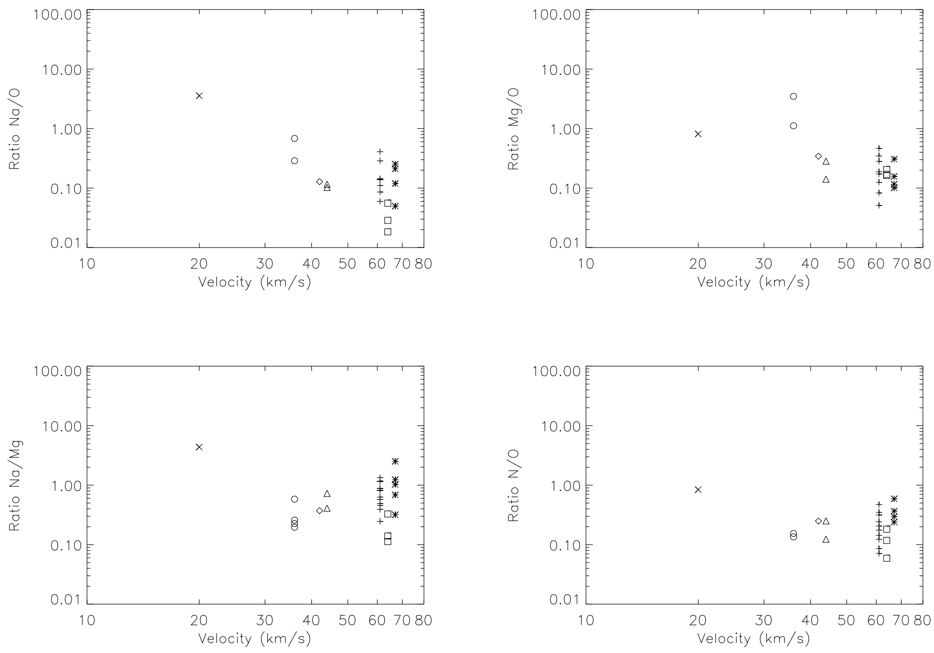

Figure 5.5: Dependence on velocity — all spectra

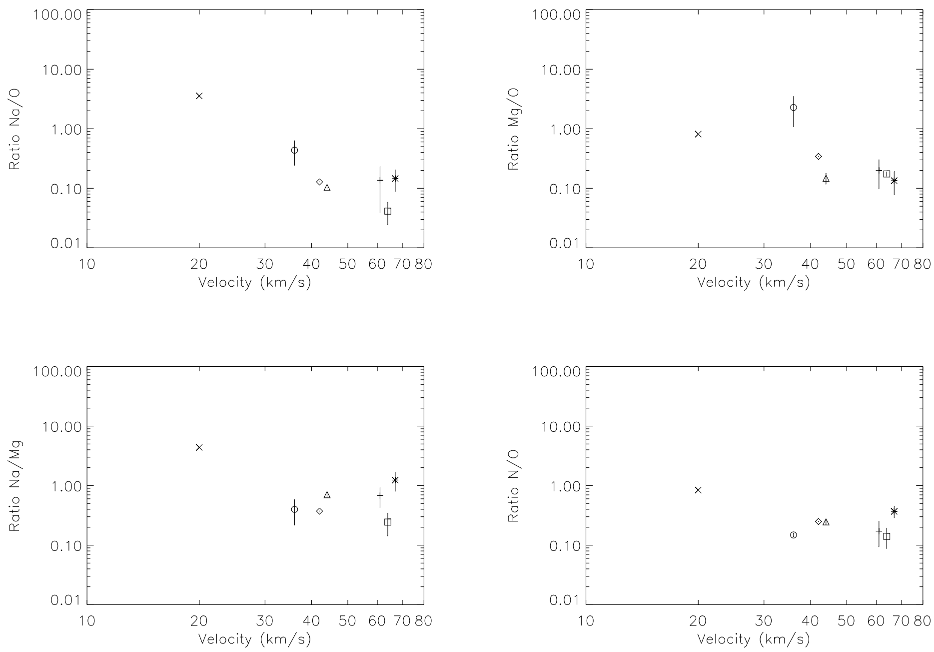

Figure 5.6: Dependence on velocity — averages

The Mg/O plots don't show clear relation. Geminids are known to have a bright Mg line. But the TVS 73 point is not sure because, as mentioned in the subsection 5.2.2, both lines are faint and the signal/noise ratio is very bad. In addition, Mg excitation potential phenomenon (see subsection 5.2.3) probably influences this plot too.

The relation of Na/Mg ratio on the velocity should be divided into two parts. In case of slow meteor Mg line isn't saturated and is optical thin (also see subsection 5.2.3). In that velocity range Na/Mg ratio decreases with increasing velocity. In the second part both lines are saturated and optically thick. Here Na/Mg ratio slightly increase with increasing velocity. The low amount of sodium in the α Monocerotids spectra is already mentioned.

The ratio N/O should be constant, independent on velocity, and this is approximately fulfilled. The TVS 73 point is uncertain, because the N line is very faint in this spectrum and thus affected by the noise.

Chapter 6

Results from TV meteor spectra

In our work we have proceeded all TV meteor spectra recorded at the Ondřejov Observatory in the time period 1990–1994. The 44 spectra which contain more than one line were selected for further analysis and statistical processing.

Our hypotheses mentioned in the Chapter 2.4 are confirmed and the expected features were really found. Also, we obtained other interested results:

6.1 Components in meteor spectra

Plots in Chapter 5 indicate differences between fast and slow meteors mentioned in Section 2.4.1.

The brightest lines of second spectrum are N I-3 (745 nm) and O I-1 (777 nm). Incidentally, whereas the bright lines of the main spectrum is a radiation of the mineral, meteoritic material, the N I-3 (745 nm) and O I-1 (777 nm) lines are atmospheric. Thus the variation of ratio of second spectrum lines is small, because the composition of Earth atmosphere is the same in all cases. But the ratio of main spectrum lines varies due to the different elemental abundance in meteoritic material.

Meteor spectrum contains not only the main and second spectrum, but also the other parts including train (forbidden line [O I] (558 nm)) and wake radiation.

The dependence of intensities ratio on velocity (plots on Fig. 5.5 or 5.6) shows interesting trends:

1. The most prominent one is decreasing trend of Na/O ratio, which confirm higher intensity of second spectrum in high velocity meteors.

2. Also Mg/O plots show similar trend but affected by the anomalous value of Geminids.

3. The Na/Mg case is a more complicated and the dependence should be divided into two velocity ranges. See Section 5.4.

4. N and O are both atmospheric lines and both become to the second spectrum. The N/O ratio should be constant and roughly speaking it is.

6.2 Peculiar features of α Monocerotids

Jenniskens et al. 1996, 1997 found that α Monocerotids penetrate deeper into the atmosphere than meteoroids of the Orionid stream or Perseid stream (meteoroids with similar velocity) and that their light curves do not show flares. The Jenniskens' results imply that α Monocerotids are more compact than other showers meteoroids and can therefore contain lower amount of volatile elements. (Section 2.4.2).

Our spectra show very low abundance of Na in all recorded α Monocerotid spectra (Sections 4.6 and 5.4) and the hypothesis concerning low amount of volatile elements could be confirmed, at least for sodium.

6.3 Peculiar features of Geminids

The parent body of Geminids is the asteroid (3200) Phaeton. So, they are supposed to be compact and have lower amount of volatile elements too. But unlike α Monocerotids (64 km/s) their velocity is only 36 km/h and the spectra should show high ratio of main/second spectrum intensity.

Our Geminid spectra really show high intensity of Mg I line (517.8 nm) relatively to the second spectrum (O I (777.4 nm)). Another main spectrum line Na I (589.2 nm) is not so bright and it is probably caused by specific Geminids composition and origin.

See Sections 4.3, 5.2.2, 5.2.3 and 5.4.

6.4 Detection of CN

Detection of CN bands on the photographs is very complicated and CN bands aren't surely demonstrated. The reasons are:

1. The dispersion of photographic spectra is high and allows to detect individual band lines. That lines are faint and lower dispersion of TV spectra is an advantage here. The individual lines aren't recognized and the cumulative brightness of band is higher.

2. It's hard to detect CN bands by observation without temporal resolution. On photograph CN bands are overlapped by N_2 bands and other lines. The TV technique allows to obtain a spectrum in the specific moment when CN bands are the brightest feature in spectral range.

We found one spectrum where CN bands are recorded, it demonstrates well the advantage of the TV recording technique. See Section 4.2.1.

6.5 Plans to the future

This work is based on the TV meteor spectra observed in 1990–1994 (plus α Monocerotids outburst 1995) which represent about one half of the spectra

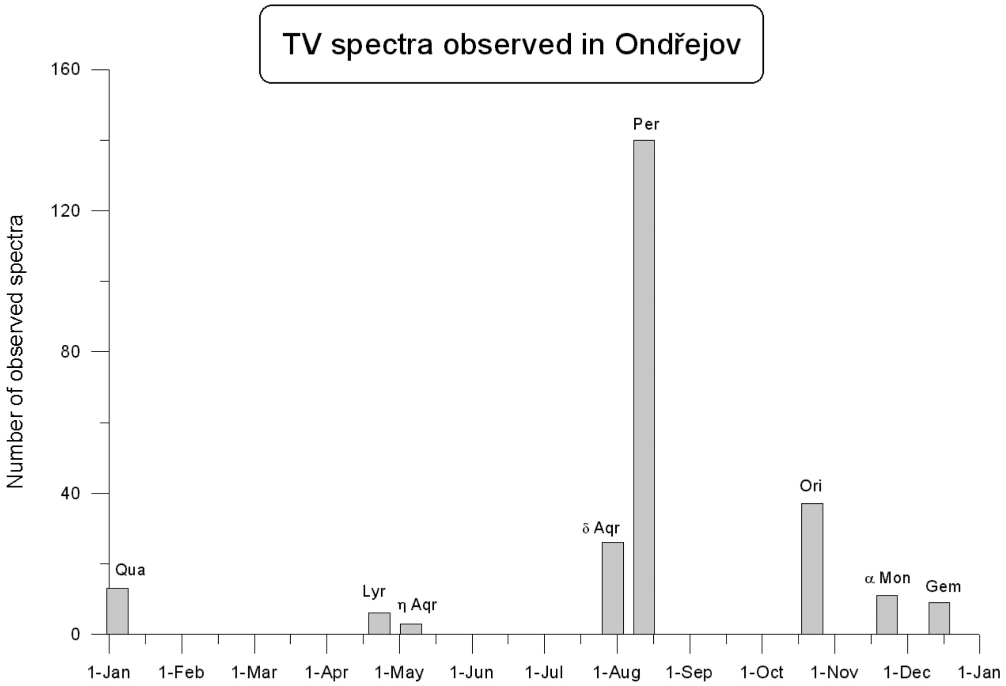

Figure 6.1: Number of TV spectra observed in Ondřejov (The numbers mean total number of spectra during observation. Sporadic meteors aren't excluded.)

taken until now. The number of all shower spectra is given in Fig. 6.1. Overview of all meteor observation in Ondřejov is summarized in the Appendix A.

So, our challenge is a digitizing and reducing of remaining spectra. We will have doubled number of data in our statistics and it should improve the credibility of our results.

As listed in Appendix A Ondřejov TV programme does not consist only of spectroscopy but also of simultaneous observation together with data collected by telescopic observers or radar and double–station observations were performed. That material could contain interesting phenomena and their investigation could bring new results.

Now we are good equipped for that work. Since January 1998 we have a new PC computer with Miro DC30 card what represents good graphic and video workstation. The quality of digitized images is now comparable to our old image processor TESLA VUST, but the new technique allows to digitize images in full PAL resolution 768×576 (TESLA VUST only 512×512). And what is more important our work is now significantly more comfortable and faster.

At present we have three cameras and we plan to observe simultaneously at two stations, making the spectral observation in Ondřejov and white light records at both stations in Ondřejov and Kunžak.

Chapter 7

Infrared spectra, color temperatures and composition of cometary dust

7.1 Comets in infrared

The infrared spectrum of comets consist in general from two parts — the region above 1 μm is dominated by the solar spectrum scattered by the about 1–10 micron–sized dust in coma, and the thermal radiation of this dust has its maximum at larger wavelengths depending on heliocentric distance of the comet.

Dust grains smaller than about 0.5 μm can not radiate effectively on longer wavelengths and so they became overheated by several tens to one hundred Kelvin when compared with the equilibrium black–body temperature at the given heliocentric distance. Larger particles, till those comparable with micrometeoroids registered in showers, have temperatures close to equilibrium but their contribution to the thermal radiation of coma could be substantial only at longer wavelengths. Thus, the thermal continuous spectrum of a coma is a mix of Planck curves of different temperatures, which is nearly planckian. The real cometary spectrum shows moreover several emission bands at 8–13, and 20, 24 μm, that are caused by silicates in grains.

Data in the long wavelength IR were obtained by IRAS (Infrared Astronomical Satellite — 1983) and now by ISO (Infrared Space Observatory) that was operating from November 1995 to April 1998.

Some preliminary methods were developed in this thesis to simulate the thermal radiation of coma and to compare it with the observed data.

7.1.1 Heat balance on small dust grains

The infrared thermal emission from the dust coma of a comet provides direct information on the size and physical composition of the dust grains and the mass loss rate from the nucleus. Strong thermal emission at 3.5 μm and 4.8 μm wavelength indicates the presence of very small ($< 0.5\,\mu$m) hot absorb-

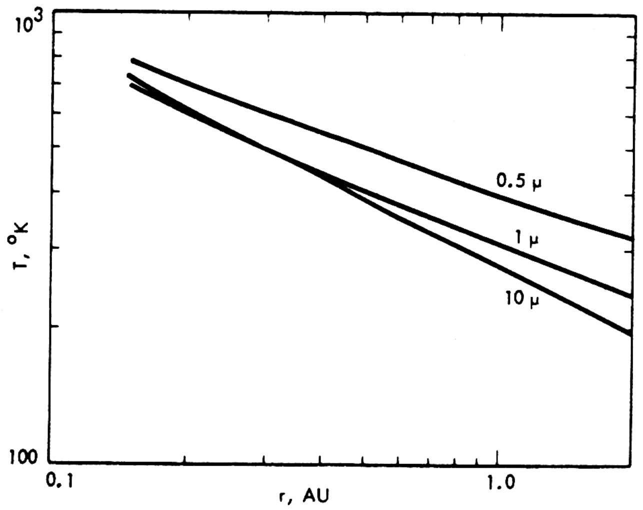

Figure 7.1: Temperature of magnetite grains vs. heliocentric distance (from Hanner 1981)

ing grains. The temperature excess above a theoretical black body at the same solar distance defines the size of the grains.

The temperature of a cometary dust grain is determined by the equilibrium between absorption of solar energy in the visible and near–infrared and thermal emission in the infrared.

$$\pi a^2 \left(\frac{r_0}{r}\right)^2 \int Q_{abs}(a,\lambda)\, S_\lambda \,\mathrm{d}\lambda = 4\pi a^2 \int \pi B_\lambda(T(a,r))\, Q_{abs}(a,\lambda)\,\mathrm{d}\lambda$$

where S_λ = solar flux at $r_0 = 1$ AU; r = heliocentric distance of comet; $B_\lambda(T(a,r))$ = Planck function at grain temperature $T(a,r)$; and $Q_{abs}(a,\lambda)$ = absorption efficiency factor computed by Mie theory from measured refractive indices. Magnetite, a mineral found in the micrometeorites collected by Brownlee (Brownlee 1977) was used here as a typical example of a strongly absorbing material. The wavelength–dependent refractive index of magnetite has been measured by Huffman and Stapp (Huffman and Stapp 1973) and Steyer, quoted in (Huffman 1977).

Computed temperatures for magnetite grains of radius 0.5 μm, 1.0 μm, and 10 μm are shown in Fig. 7.1 as a function of heliocentric distance. The small grains are hotter than a rapidly rotating black body at the same heliocentric distance, because they do not radiate efficiently at infrared wavelengths ($\lambda \gg a$). A 0.5 μm grain is by $\approx$ 100 K hotter than a 1.0 μm grain at the same heliocentric distance; a grain of radius 0.3 μm will be by $\approx$ 200 K hotter than a 1.0 μm grain. If submicron absorbing grains are abundant in the dust coma, therefore, their presence should be detectable in the infrared. The temperature of absorbing grains larger than 10–20 μm converges towards the temperature of a black body.

(According to (Hanner 1981).)

7.1.2 10 μm "silicate feature"

The range 8–13 μm is the most important part of the infrared mineral spectrum. The shape of 10 μm peak indicates a chemical composition of a source. This shape strongly depends on presence of pyroxene, olivine, layer smectite or glass. Fig. 7.2 shows the 10 μm "silicate feature" of four crystalline mineral standards: (a) orthoenstatite ($MgSiO_3$), (b) clinoenstatite ($MgSiO_3$), (c) forsteritic olivine (Mg_2SiO_4), and (d) layer lattice silicate (smectite). The positions of the strongest bands are indicated in wavenumbers (vertical scale = transmittance). From (Bradley 1992).

7.1.3 IR spectra and analytical electron microscopy (AEM) of IDP's

The IR spectra and AEM results of IDPs are shown in this section. Interplanetary Dust Particles (IDPs) are small (typically 5–50 μm in diameter) particles collected in stratosphere (at 20–25 km altitude) using e.g. the U–2 aircraft (Sandford 1985). One of analysed IDPs is shown on Fig. 7.3. Note the high porosity and fragile, aggregated microstructure of this particle.

IR spectra were obtained from thin (<100 nm) sections. AEM measuring on 200–700 points on each section yields relative abundances of olivine, pyroxene, layer silicates, and glass. The comparison of IR spectra and AEM chemical composition is very important for interpretation of non–laboratory IR observations.

Pyroxene–rich IDPs The 10 μm "silicate feature" of the pyroxene–rich IDPs (Fig. 7.4) consists of two principal bands at 9.1–9.4 μm (1064–1099 cm^{-1}) and 10.5–10.75 μm (930–953 cm^{-1}). The bands are consistent with monoclinic clinopyroxene whose presence in the thin sections was confirmed using AEM.

Fig. 7.4 shows: (A–C) IR spectra from thin section of IDPs (vertical scale = transmittance). (D–F) Corresponding Mg–Fe–Si ternary plots (atom %). "PY" and "OL" denote compositional tie lines for pyroxene ($MgSiO_3$–$FeSiO_3$) and olivine (Mg_2SiO_4–Fe_2SiO_4) respectively. Clustering of data points about an Mg–rich pyroxene (enstatite) composition indicates that all three IDPs are pyroxene–rich.

Olivine and smectite –rich IDPs The olivine–rich IDPs (Fig. 7.5) produce an intense silicate band at 11.2–11.3 μm (885–893 cm^{-1}), with less intense bands at 10.1 and 10.75 μm (930, 991 cm^{-1}), while the layer silicate–rich IDP (Fig. 7.6) produces a principal silicate band at $\approx$9.8 μm (1031 cm^{-1}). (An additional band at 6.8 μm (1471 cm^{-1}) indicates the presence of carbonates in that particle.)

On Fig. 7.5 are: (A–B) IR spectra from thin sections of IDPs (vertical scale = transmittance). "cpx" and "ol" in A indicate clinopyroxene and olivine absorption bands. (C–D) Corresponding Mg–Fe–Si ternary plots (atom %). "PY" and "OL" denote the compositional tie lines for pyroxene ($MgSiO_3$–$FeSiO_3$) and

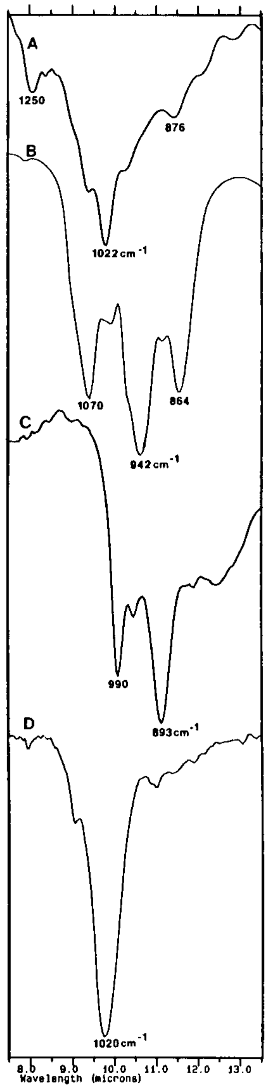

Figure 7.2: IR spectra of mineral standards

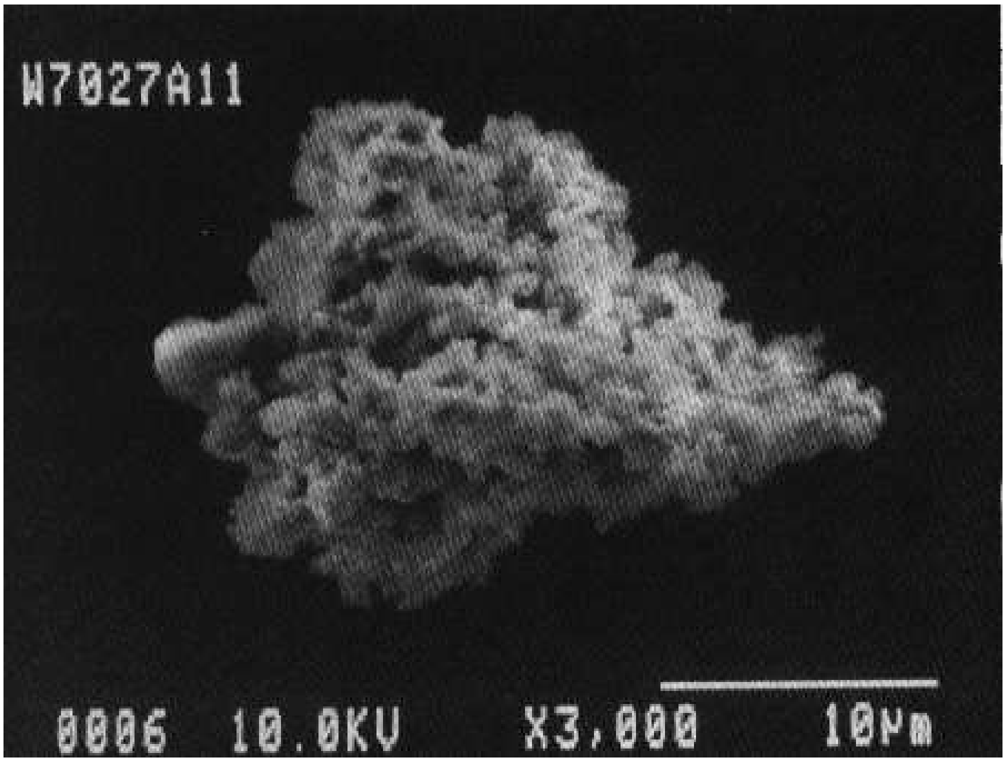

Figure 7.3: Typical shaped (glass–rich chondritic) IDP

olivine (Mg_2SiO_4–Fe_2SiO_4) respectively. Concentrations of data points on the olivine tie line indicate that olivine is the dominant silicate in both IDPs.

And Fig. 7.6 shows: (A) IR spectrum of the layer silicate (smectite)–rich IDP (vertical scale = transmittance). The strongest band (peaked at $\approx$9.8 μm) is the silicate feature, and the $\approx$6.8 μm band corresponds to the carbonate asymmetric stretching vibration. (B) Corresponding Mg–Fe–Si ternary plots (atom %). Distribution of data points reflects the mixing of the three major components of this thin section, Mg–rich smectite (*solid boxed area*), Mg–Fe carbonates (*dotted area*), and Fe sulfides (*dashed area*).

Glass–rich IDPs The most interested spectra are the ones of glass–rich IDPs (Fig. 7.7 — (A–B) IR spectra from thin sections of the glass–rich chondritic IDPs (vertical scale = transmittance). (C–D) Corresponding Mg–Fe–Si ternary plots). The glass–rich IDPs produce broad silicate band structure between 8 and 12 μm, with a prominent peak at 11.3 μm.

The 10 μm silicate features of the olivine, pyroxene, and layer silicate –rich IDPs are unlike those of comets, but those of glass–rich are similar to comets like Halley and Bradfield in terms of overall bandwidth and shape, as well as the 11.3 μm "olivine" feature (compare Fig. 7.8). Chondritic IDPs dominated by glass and submicrometer silicate crystals are strong candidates for the dust grains responsible for silicate IR emission from comets.

Comparison of the silicate emission characteristics of comets and glass–rich IDPs (Fig. 7.8) shows: (a) Comet Bradfield (1987s) divided by the continuum

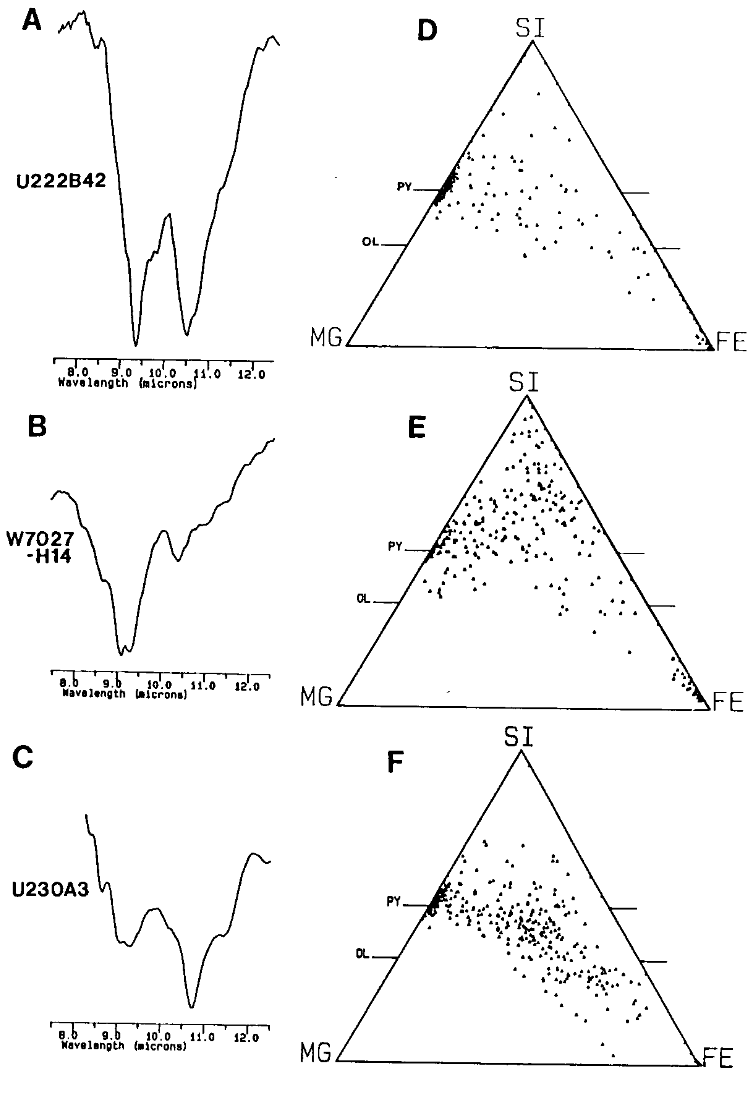

Figure 7.4: IR spectra and AEM of pyroxene–rich IDPs

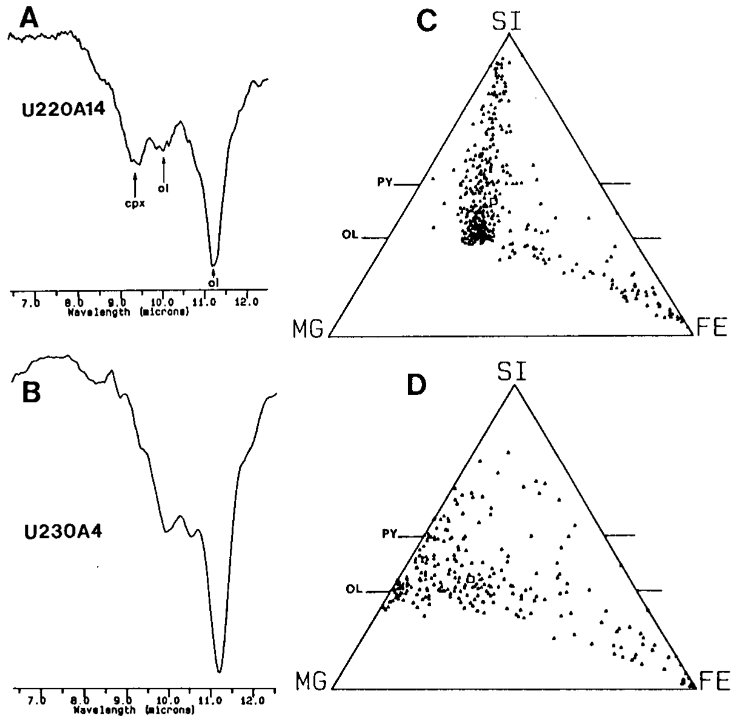

Figure 7.5: IR spectra and AEM of olivine–rich IDPs

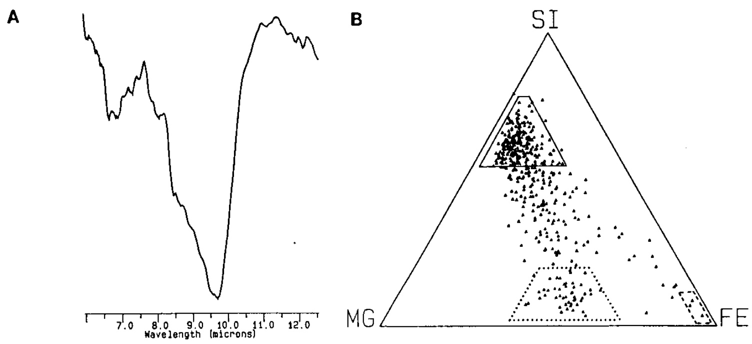

Figure 7.6: IR spectra and AEM of layer silicate (smectite)–rich IDP

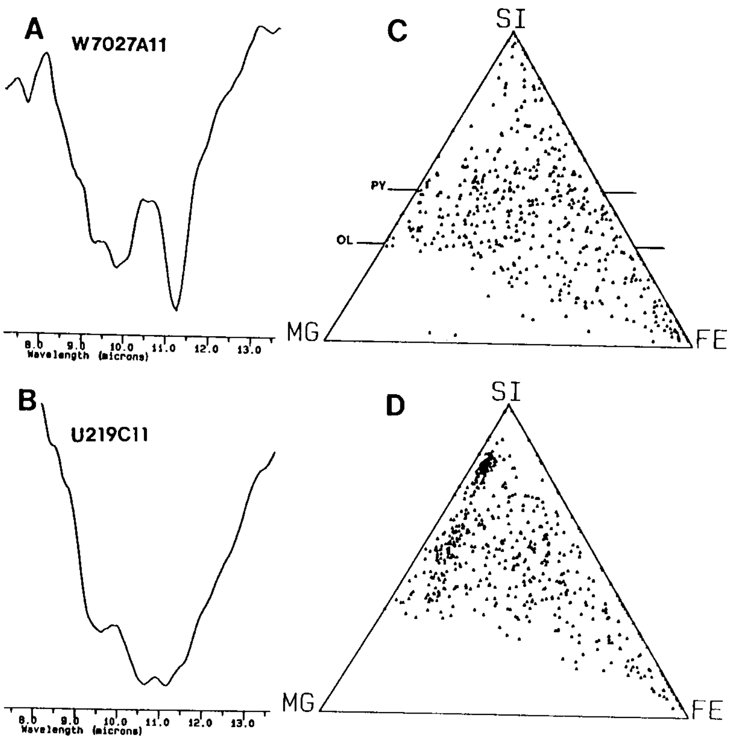

Figure 7.7: IR spectra and AEM of glass–rich IDPs

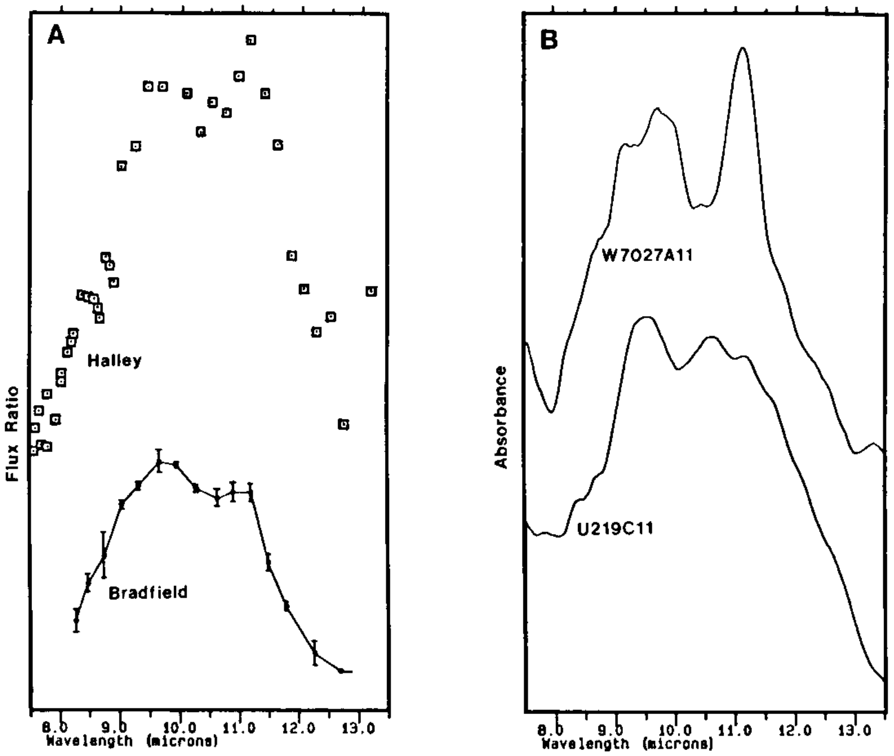

Figure 7.8: Comparison of cometary and IDPs' IR spectra

and normalized at 12.81 μm (from Hanner et al. 1990). Comet Halley (December 1985) divided by a 320 K black body continuum and normalized at 6.0 μm (from Bregman et al. 1987). (b) Glass–rich chondritic IDPs.

(All figures in this subsection from (Bradley 1992))

7.1.4 $Af\rho$ parameter

In order to quantify the production of dust grains from the continuum data, the $Af\rho$ parameter was introduced by A'Hearn et al. (1984):

$$Af\rho = \frac{(2r\Delta)^2}{\rho}\frac{F_c}{F_\odot}$$

where A is the albedo of the grains, f the fraction of the telescope field of view (aperture) filled or obscured by the dust grains in the comet, ρ the projected radius in the sky of the aperture used for the photometry (in km), r the comet's heliocentric distance (in AU), Δ the comet's geocentric distance (in km), F_c the measured continuum cometary flux and $F_\odot$ the solar flux at 1 AU.

If the continuum brightness follows a ρ^{-1} power law (uniform outflow), the column density therefore varies as $1/\rho$, and then the $Af\rho$ parameter is proportional to the dust production rate.

In the simplest model for cometary activity, the gas–to–dust ratio reflects the nuclear volatile–to–refractory ratio.

In the fitting code the $Af\rho$ parameter was replaced by optical depth τ of the dusty coma, that express the same quantity. It allow to use the same code also for completely opaque solid bodies like Chiron, if τ is set e.g. > 10. The parameter radius expressed the radius of the asteroid in this case instead the radius of the coma. T_{mode} introduces the difference between a fast, slow and rotation of the object.

7.2 ISOPHOT observations

Infrared photometrical observations of several comets and cometary–like objects were included in the Guaranteed time programme by ISOPHOT: 29P/Swassmann–Wachmann 1, 22P/Kopff, (2060) Chiron; and the comet C/1995 O1 Hale–Bopp became a very suitable bright object of the Target of Opportunity programme. Most of the photometric observations were accompanied by SWS/LWS spectrometry as close as possible to the observing dates of ISOPHOT. Unfortunately the great comet of the year 1996 Hyakutake could not be observed due to its fast proper motion.

The sequence of ISOPHOT observations consisted of photometry with some of broad–band filters 3.6, 7.3, 10, 12.8, 16, 25, 60, 100, 160 μm, using several apertures at 16 and 25 μm filters; and chopping between the comet and internal calibration heat source. In order to extract the infrared background, one more observation was done at the same position with the same filters, apertures and exposure times, but some days later, when the comet already moved to another place (so called shadow observation).

7.2.1 Comet Kopff

Figs. 7.9 and 7.10 show the observed data on March 6 and 14, 1996 together with fitted Planck curve. Parameters of curves are listed in the figures. An albedo value 0.05 and radius of coma 3 000 km were used. The τ and T_{mode} parameter were set to fit the spectrum. τ would be 0.0001 for diluted coma and 10.0 for bare nucleus. T_{mode} would be 390 K for subsolar point, 330 K for slowly rotating object and 280 K for fast rotating object.

The observations were also performed by other instruments (ISOCAM) and the cometary trail was detected by comet Kopff. The Kopff trail was observed close to the maximum visible brightness of the comet, at 4 distances from the nucleus along the cometary path: -2 degrees, $+0.25$, 2 and 5 degrees. Scans at these distances perpendicular to the trail were performed.

Cometary trails were found for the first time on IRAS pictures in 1983, they resemble wires in the space along the cometary orbits. As it was soon interpreted, they consist of millimeter to centimeter sized solid particles released from cometary nucleus. Since these particles are much larger than the dust in coma, they are not influenced comparatively by the solar radiation pressure and they remain in the interplanetary space near to the orbit of their source comet.

The millimeter to centimeter sized particles are the ones which cause the faint meteors observed by TV technique (spectroscopy) as described in the previous Chapters.

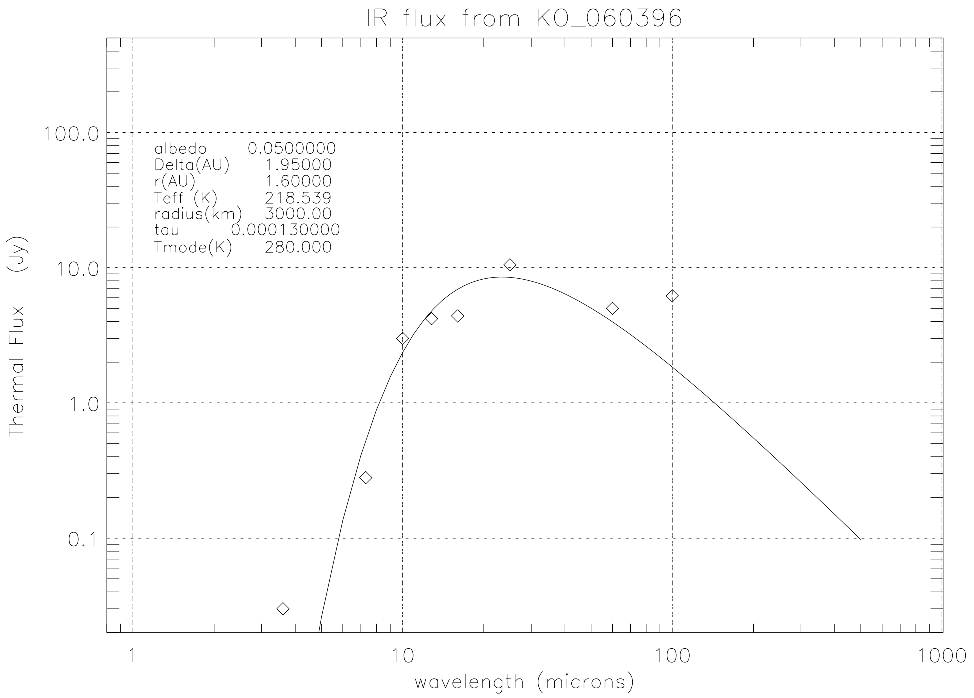

Figure 7.9: Comet Kopff, March 6, 1996

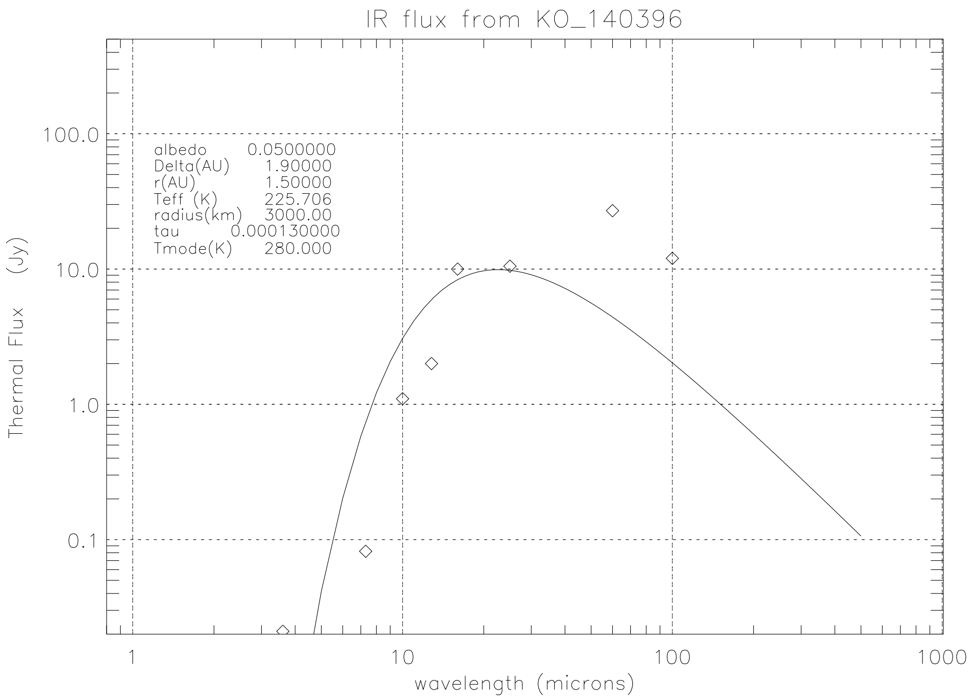

Figure 7.10: Comet Kopff, March 14, 1996

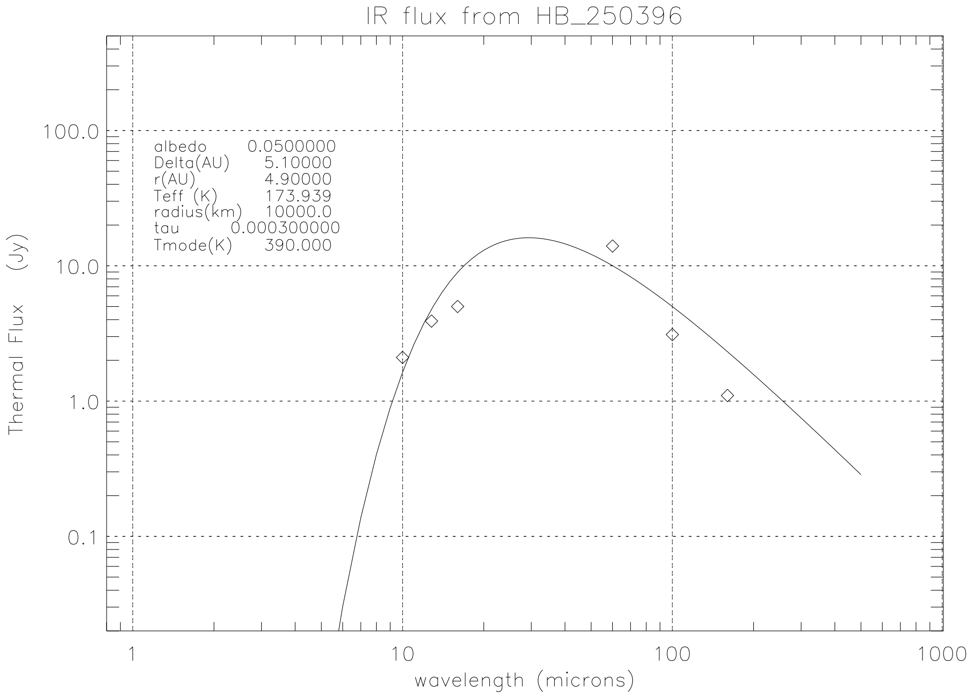

Figure 7.11: Comet Hale–Bopp, March 25, 1996

7.2.2 Comet Hale–Bopp

Comet Hale–Bopp was the great comet of 1997. The early discovery and its strong activity at large heliocentric distance provided a rare opportunity to observe the dust over a wide range in solar heating.

Figs. 7.11, 7.12, 7.13, 7.14, 7.15 show the ISOPHOT observations together with Planck curve. Parameters of curves are listed in the figures. In the case of Comet Hale–Bopp we use higher value of coma radius — 10 000 km. The same albedo value as in the case of Comet Kopff — 0.05 was used. Similarly as in the Section 7.2.1, the τ and T_{mode} parameter were set to fit the spectrum. τ would be 0.0003 for a diluted coma. T_{mode} would be 390 K for subsolar point, 330 K for slowly rotating object and 280 K for fast rotating object.

The measured intensity on 3.6 μm (Figs. 7.13, 7.14 and 7.15) is very high but note that we measure the scattered solar light at this wavelength, not only thermal radiation of dust.

In all cases when observations with 25 μm filter were performed (Figs. 7.12, 7.14 and 7.15) the measured value was significantly higher than the corresponding Planck curve.

This discrepancy can be explained by other observation — measurement of SWS (Short Wavelength Spectrometer). Fig. 7.16 shows the observed spectrum together with a modelled spectrum of forsterite (Mg–rich olivine). It is a dramatic confirmation of the olivine identification. Olivine produces the peak around 25 μm that causes the higher value in the observed spectrum of comet

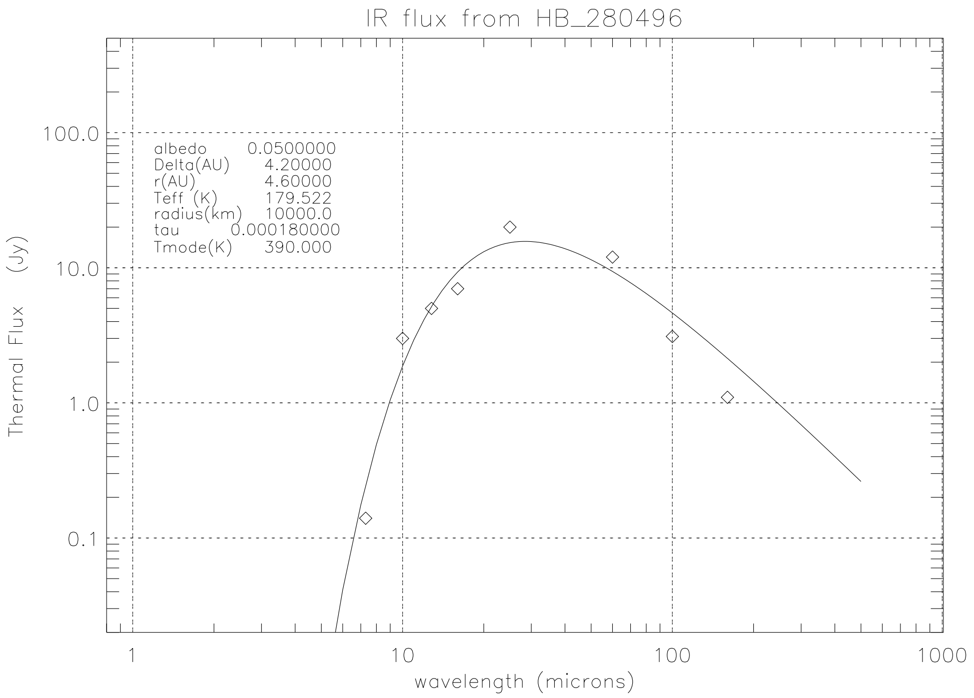

Figure 7.12: Comet Hale–Bopp, April 28, 1996

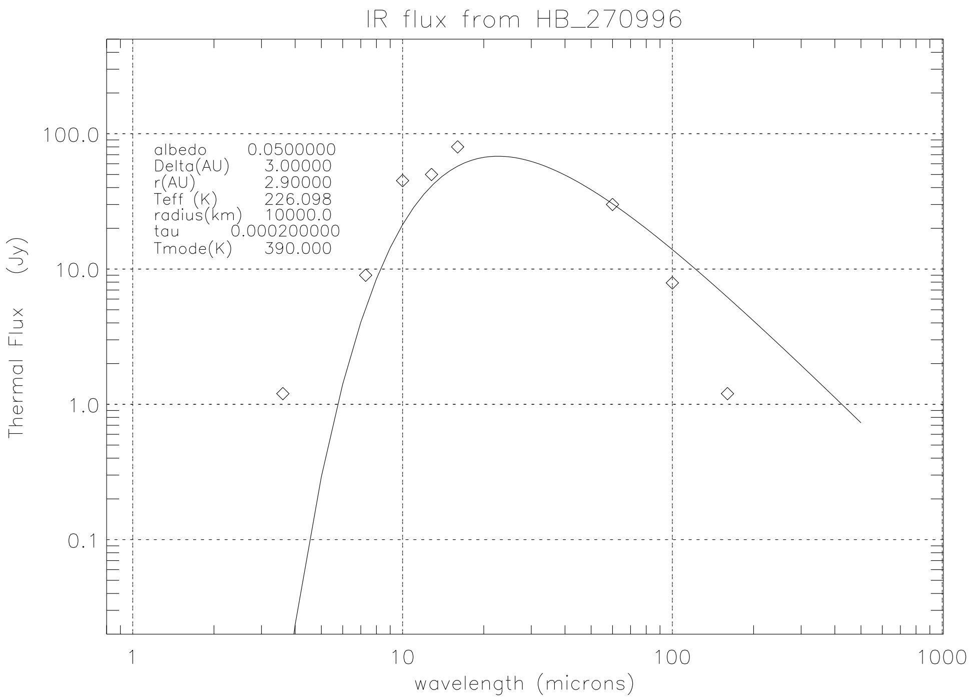

Figure 7.13: Comet Hale–Bopp, September 27, 1996

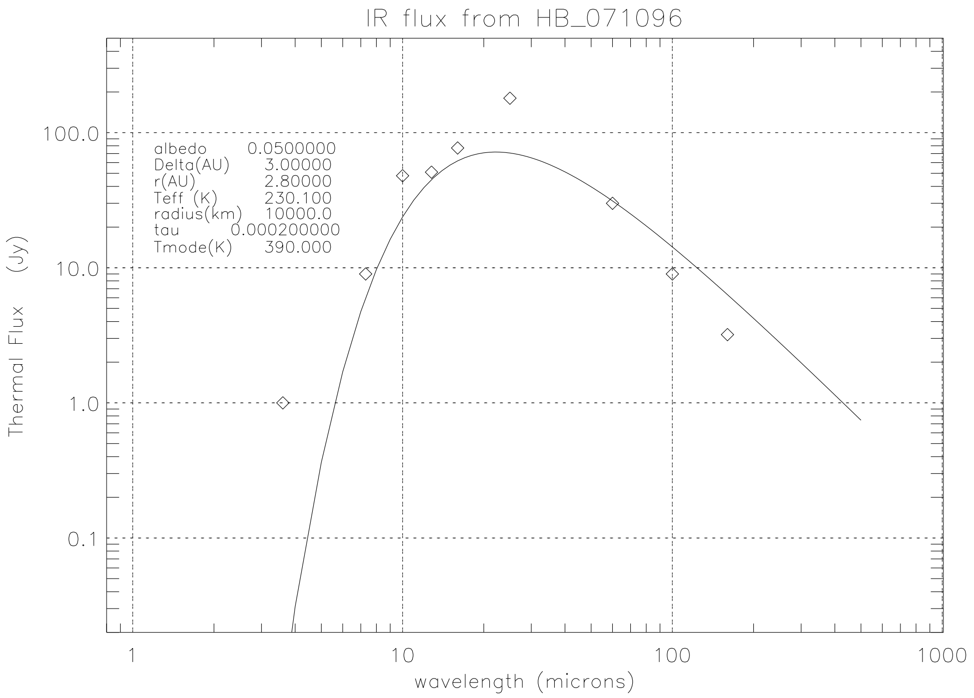

Figure 7.14: Comet Hale–Bopp, October 7, 1996

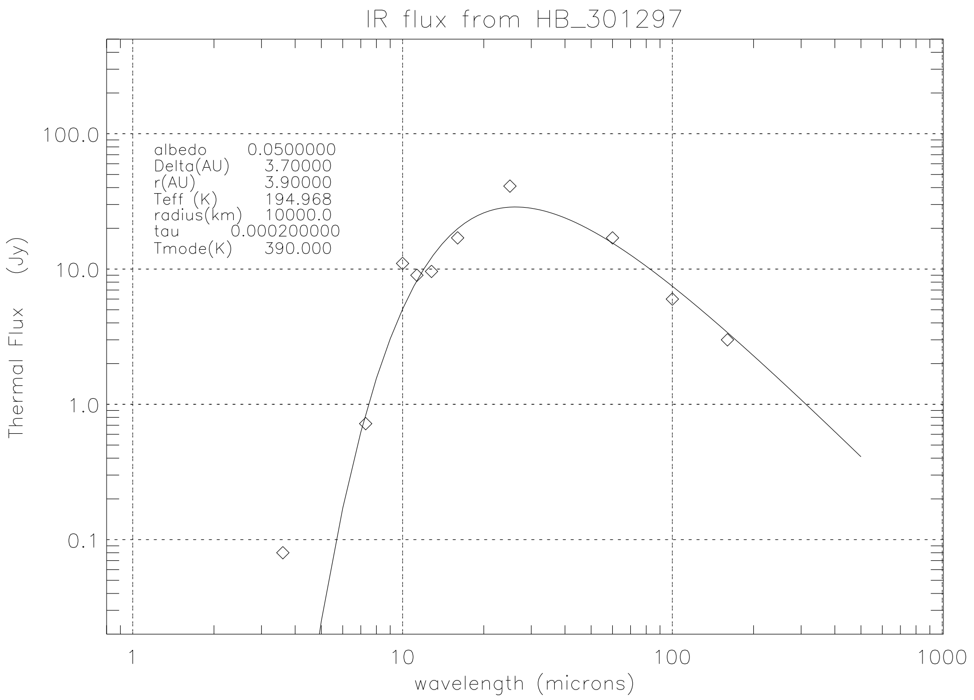

Figure 7.15: Comet Hale–Bopp, December 30, 1997

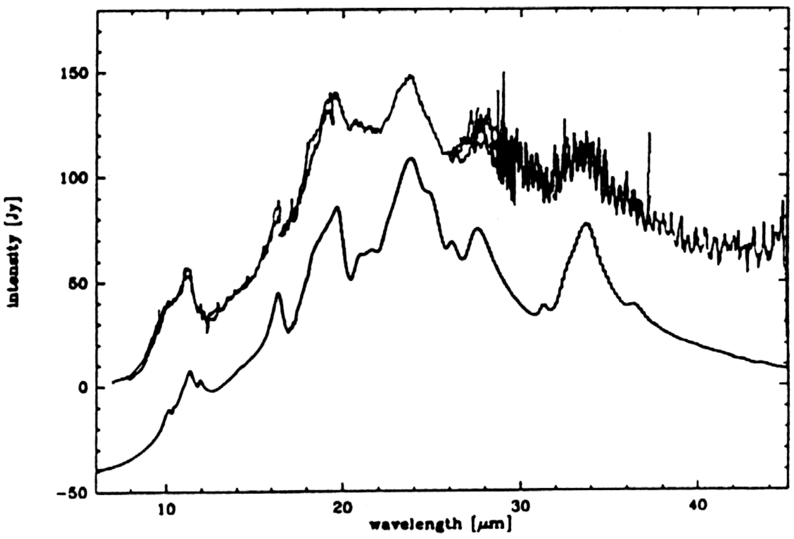

Figure 7.16: ISO SWS spectrum of Hale–Bopp October 6, 1996 (upper curve) and a modelled spectrum of forsterite (lower curve), (Crovisier et al. 1997)

Hale–Bopp.

7.3 Model of the dust distribution in coma

Infrared photometric observations of comets 22P/Kopff, 29P/Swassmann–Wachmann 1 and 2060 Chiron were proposed in frames of Guaranteed Time ISO programme by Gruen E. et al. and also of comet C/1995 O1 (Hale–Bopp) was accepted as Target of Opportunity cometary object. The ISOPHOT multifilter and multiaperture absolute photometry supplied data that can be compared with some kind of dust coma model, e.g. like that by Lutz Massone (Massone 1985, 1987). Based on the space distribution of dust within the coma and on some presumed optical properties of dust grains, his model integrates the one–times scattered sunlight along the lines of sight through the coma and produces synthetic visual images that can show well e.g. near nucleus structures within the coma. In addition to this, our presented dust coma model for ISOPHOT photometry allows to produce synthetic images of thermal radiation by dust grains of different sizes and temperatures and to integrate it over the ISOPHOT apertures. Examples of synthetic thermal radiation IR images of some characteristic structures like rotating jet, dust shell after outburst etc. will be presented as complementary to the visual images of these structures (Štork & Šolc 1996).

7.3.1 Program COMETBOX

In addition to the models of dust distribution in coma we produce the program for computing the image of coma.

The aim of our modelling is to produce images in arbitrary spectral range. The programme inputs are:

- dust distribution — six matrixes containing the space distribution of 0.5, 1.0, 1.5, 2.0, 2.5, 3.0 μm dust grains (the number of particles per volume element)
- temperatures of 0.5, 1.0, 1.5, 2.0, 2.5, 3.0 μm dust grains
- requested spectral range (λ_a, λ_b) or tabulated filter function

We assume an optical thin coma so that we can integrate the radiation by simple addition of radiation along line of view. The radiation is computed according to the Planck law

$$planck(\lambda, T) = \frac{2hc^2}{\lambda^5} \frac{1}{e^{\frac{hc}{k\lambda T}} - 1}$$

(where $h = 6.6 \cdot 10^{-34}$ J s is Planck constant, c velocity of light and $k = 1.4 \cdot 10^{-23}$ J K^{-1} is Boltzmann constant) using integration by rectangular method from λ_a to λ_b. In case a filter function is given, programme integrates through a non–zero filter transmittance.

The output of our programme is a matrix containing an image in requested spectral range.

For complete and commented list of program COMETBOX see Appendix D.

Displaying and supporting utilities

For a visualization of computed images some utilities were developed. Although I wrote the programme COMETBOX in FORTRAN, I prefer IDL for those utilities. The COMETBOX code in FORTRAN allows run it as stand–alone programme on various (MS DOS, UNIX) computers. In higher resolution of a box and images, the programme requires megabytes of memory and hours of a machine time. On the other hand the visual routines should be written in IDL. IDL (Interactive Data Language) is standard environment for ISO programs and the ISO service software is written in IDL too.

Test example

To show the ability of the programme and differences of images in different spectral ranges, we generated test dust distribution keeping the following conditions:

- Larger particles are more concentrated to the nucleus than smaller ones.
- Smaller particles are shifted into the tail direction.

size	temperature
0.5 μm	400 K
1.0 μm	300 K
1.5 μm	285 K
2.0 μm	270 K
2.5 μm	260 K
3.0 μm	250 K

Table 7.1: Temperatures of test particles

The smaller dust particles are known to have higher temperature than bigger ones. Temperatures of test particles we used are listed in Tab. 7.1.

The spatial resolution of the test model was $30 \times 30 \times 30$ cells and so resolution of the resultant images is 30×30 pixels.

The computation in above mentioned resolution is relatively fast, takes only minutes of computer time and requires only about one megabyte of memory.

7.3.2 Comparison of coma images using different spectral filters

Images in nine spectral ranges were computed by our programme. Views in the ISO spectral filters 3.6, 7.3, 10, 12.8, 16, 25, 60, 100 and 160 μm are shown in Fig. 7.17. The used spectral filters are also described.

Spectral filters

The space probe ISO is equipped by the set of spectral filters 3.6, 7.3, 10, 12.8, 16, 25, 60, 100 and 160 μm. For our computation we use the transmittance profiles of those real filters as shown in Fig. 7.18.

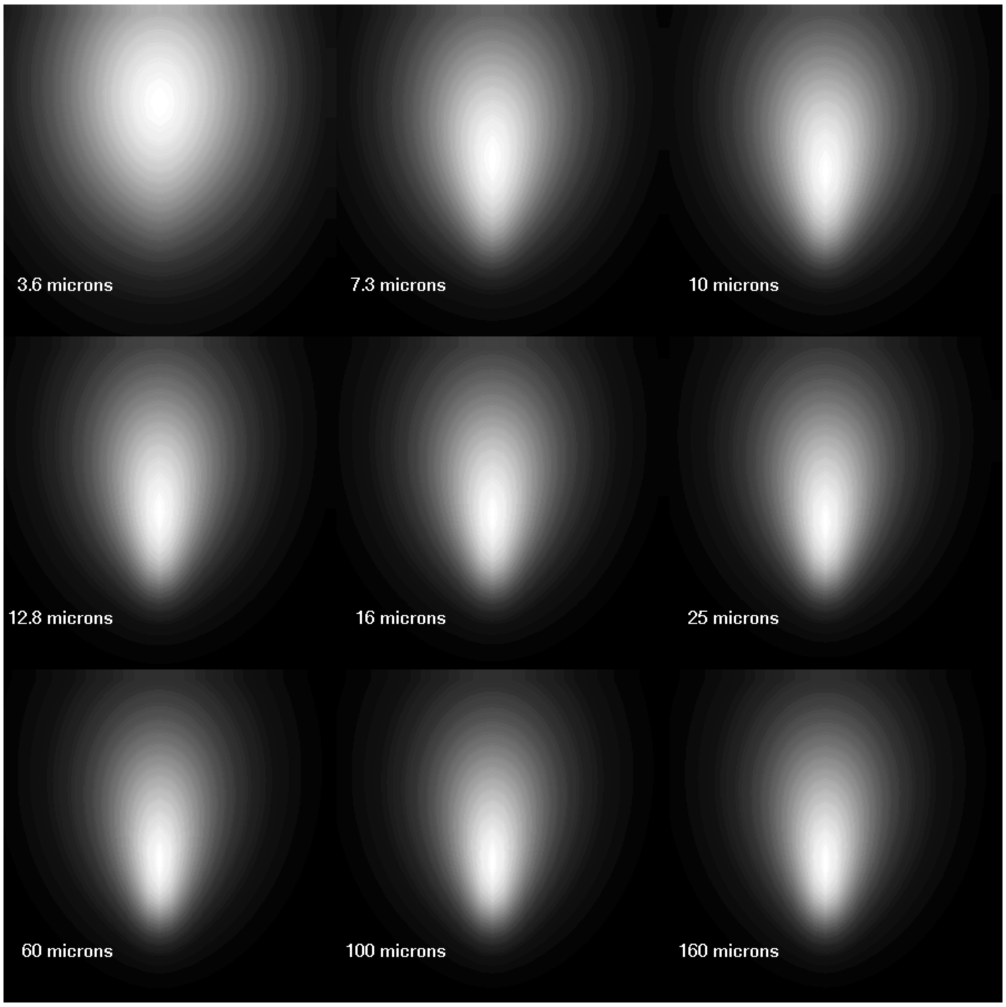

Figure 7.17: View of test particles in various spectral filters

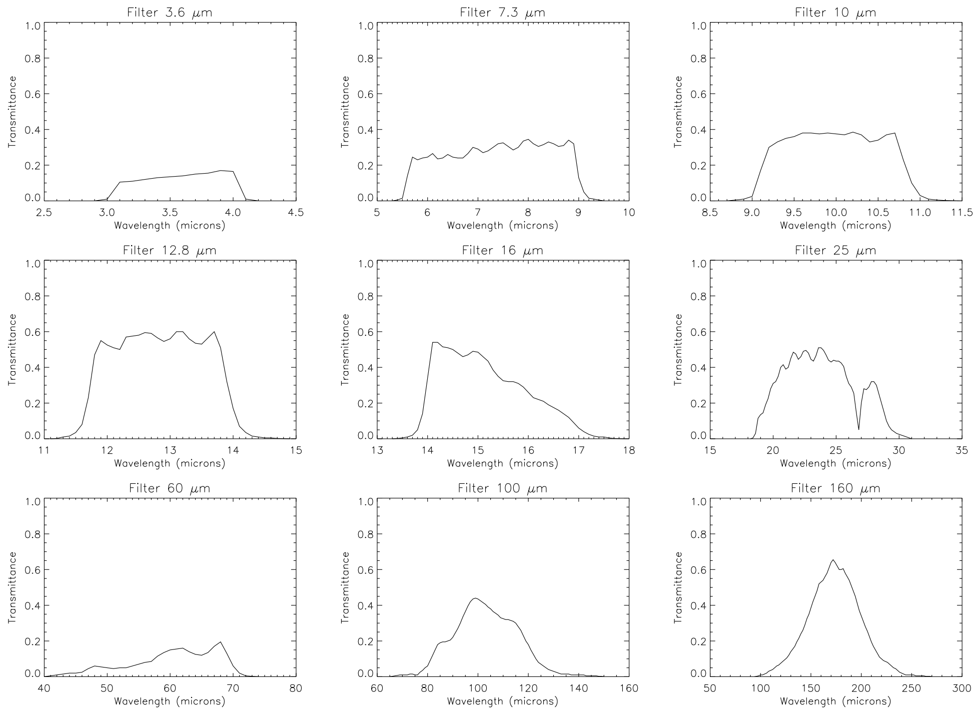

Figure 7.18: Transmittance profiles of used spectral filters (ESA 1994 — ISOPHOT)

Chapter 8

Conclusions

We processed meteor spectra observed on the Ondřejov observatory during the period 1990–1994. Elaboration of 44 high quality spectra allow us to analyze statistical dependencies, especially the dependence of spectrum features on the velocity. As mentioned in Chapter 6, the most important results are:

- Confirmation that the second spectrum is more intensive in case of higher meteoroid velocity
- Low abundance of Na in α Monocerotids which implies a compactness of that material (Štork et al. 1998)
- Specific composition and origin of Geminids
- Detection of CN bands

The analyzing of ISO data continues. ISOPHOT observed also those solid cometary particles which are bigger then dust observed in the visible light.

The absolute photometry of comets observed by ISOPHOT in the range 3–200 μm unambiguously shows that temperature of dust grains depends not only on their albedo and hence on their material, but also on their size. The Planck curves fitted on the observed data can be affected by the presence of silicate bands on 10, 20 and 24–25 μm. If satisfactory fit around maximum of curve (around 10 μm) is found, then the Planck curve represents mainly the temperature of smaller particles.

More informations about the distribution of temperatures, abundance of bigger, millimeter sized particles can probably be obtained by analyzing data from experiments SWS and LWS and by using theory which describe thermal radiation of small particles better than the Planck law. The important result will be the estimation of the abundance and composition of these bigger particles in coma which can be compared with the abundance and composition of particles in the cometary trails (as observed in comet Kopff by ISOPHOT) and in the meteoritic streams as results from radar and TV meteor observations.

Appendix A

Overview of TV meteors observed till the end of 1997

Appendix B

Infrared astronomy from space (IRAS definitions)

B.1 Infrared units

The infrared wavelength range has borrowed units from the adjacent optical and radio (submm) regimes. Both magnitude and flux representations are widely used.

Flux density F_ν of a source is defined as the flux per unit frequency. Flux density is the physical unit used for point sources. The unit of flux density is $\mathrm{W\,m^{-2}Hz^{-1}}$. For practical purposes in the infrared it is often convenient to scale this SI unit using Jansky instead of it.

$$1 \text{ Jy} = 10^{-26} \text{ W m}^{-2}\text{Hz}^{-1}$$

For extended objects, the surface brightness B_ν is equivalent to the flux density. Brightness is defined as the flux density per unit solid angle. The unit of brightness is $\mathrm{W\,m^{-2}Hz^{-1}sr^{-1}}$, but in practice it is often scaled to $\mathrm{MJy\,sr^{-1}}$:

$$1 \text{ MJy sr}^{-1} = 10^{-20} \text{ W m}^{-2}\text{Hz}^{-1}\text{sr}^{-1}$$

Flux density of a point source, in particular for a stellar object, is often given in magnitudes m. In the ISO wavelength range, these units are mostly used for ground based measurements below 20 μm. The conversion to or from magnitudes is performed via zero magnitude flux density F_0, which depends on the wavelength and the photometric system used. Zero magnitude flux densities for ESO infrared filters J through Q are listed in Table B.1. $\mathrm{N_1}$, $\mathrm{N_2}$ and $\mathrm{N_3}$ are narrow band filters to trace the dust features around 10 μm.

Magnitude m of a ground based observation can be converted into flux density with formula

$$F_\nu = F_0\,10^{\frac{m}{2.5}}.$$

For spectroscopic measurements, the total flux F of a line is often the most interesting quantity. A flux calibrated spectrum may be presented in the form of flux density F_λ as a function of wavelength λ. Flux F of a line in interest can be obtained by subtracting an appropriate continuum flux density level of

Filter	λ (μm)	$\Delta\lambda$ (μm)	F_0 (Jy)
J	1.24	0.2	1587
H	1.64	0.3	1074
K	2.18	0.4	653
L′	3.76	0.7	253
M	4.69	0.5	150
N	10.3	5.2	29.4
N_1	8.38	0.8	48.7
N_2	9.67	1.6	34.9
N_3	12.9	3.7	19.7
Q	18.6	5.6	9.5

Table B.1: Zero magnitude flux densities in the ESO infrared filters

the spectrum before integrating over the entire line in wavelength λ. The unit of flux is $\mathrm{W\,m^{-2}}$.

B.2 Absolute calibration

The absolute calibration of the point source observations is tied directly to the absolute calibration of the ground based photometric system at 10 μm. The 12 μm band is calibrated via measurements of α Tau. Extrapolation to the 25 and 60 μm bands is achieved using models of stars, normalized to observation of the Sun. The extrapolation of the absolute calibration from 60 to 100 μm is based on observations and model calculations of asteroids whose absolute flux at 60 μm was obtained using the stellar calibration.

B.2.1 Stellar calibration

The absolute calibration at 12 μm was set so that the flux density of α Tau at that wavelength was 448 Jy.

In order to extrapolate the absolute calibration which was established for the 12 μm band to the longer wavelengths, it is convenient to define a magnitude system for inter–comparisons of the photometry in different wavelength bands. Since the energy distribution of the stars is very nearly black body, the magnitude system has been defined such that the zero magnitude corresponds to a flux density in Janskys:

$$f_\nu(0.00\,\mathrm{mag}) = 1.57 \cdot 10^{-16} \times B_\nu(10\,000\,\mathrm{K})$$

where B_ν is the Planck function in $\mathrm{Jy\,sr^{-1}}$. For the IRAS effective wavelengths $f_\nu[0.00\,\mathrm{mag}]$ is 28.3, 6.73, 1.19 and 0.43 Jy at 12, 25, 60 and 100 μm respectively. The stars used to develop the calibration are listed in Table B.2 with the resulting magnitudes from IRAS observations.

Star	[12 μm] (mag)	[25 μm] (mag)	[60 μm] (mag)
α Tau	-3.00	-2.97	-2.95
α Aur	-1.91	-1.91	-1.86
α Car	-1.40	-1.38	-1.33
α CMa	-1.36	-1.32	-1.27
α CMi	-0.74	-0.72	-0.70
β Gem	-1.20	-1.18	-1.17
α Leo	1.66	1.72	—
α Boo	-3.15	-3.10	-3.11

Table B.2: IRAS magnitudes of calibration stars

Asteroid	Color Temp. (K)
Europa	228$\pm$15
Bamberga	243$\pm$10
Hygiea	232$\pm$16

Table B.3: Color temperatures of asteroids between 25 and 60 μm

B.2.2 Asteroid calibration

The fluxes from the asteroids Hygiea, Europa and Bamberga were observed. Color temperatures were derived for each observation using the stellar calibration at 25 and 60 μm, and the assumption was then made that these color temperatures would remain unchanged between 60 and 100 μm. The flux at 100 μm was then calculated from the appropriate blackbody function and the stellar calibration at 60 μm. The average of the predicted 100 μm fluxes for the three asteroids was then adopted as the basis of the 100 μm absolute calibration. The average color temperatures are given in Table B.3.

Appendix C

Infrared Space Observatory — ISO

Infrared Space Observatory is an ultimate infrared space telescope (launched November 17, 1995 — switched off on May 16, 1998). The main ISO advantages in comparison to previous IR satellite IRAS (Infrared Astronomical Satellite) are:

- ISO observes on larger interval of wavelengths 3–200 μm. IRAS observed only on four discrete wavelengths 12, 25, 60 and 100 μm.
- A better sensitivity of ISO detectors. They are approximately ten times more sensitive than IRAS's ones.
- IRAS mainly scanned the sky, ISO was a 3–D pointed satellite able to follow moving sources too. can be pointed on one source.

C.1 Satellite

The satellite was a large cryostat containing over 2000 litres of liquid helium for cooling the telescope to temperatures between 2 and 8 K. A nominal lifetime was 18 months. Dimensions of satellite were: height 5.3 m, width 3.6 m and depth 2.8 m. Its mass was 2200 kg. The ISO spacecraft is shown in Fig. C.1.

The ISO telescope was a 60 cm diameter Ritchey–Chrétien system with a focal ratio of f/15. ISO payload consisted of four instruments:

- a camera: CAM, 2.5 – 17 μm
- an imaging photo–polarimeter: PHT, 2.5 – 240 μm
- a short wavelength spectrometer: SWS, 2.5 – 45 μm
- a long wavelength spectrometer: LWS, 43 – 196.7 μm

The 3 arcmin field of view of each instrument was at an angle of 8.5 degrees from the telescope optical axis. All four instrument fields of view were centered around this axis. Because the four instruments viewed separate areas of the

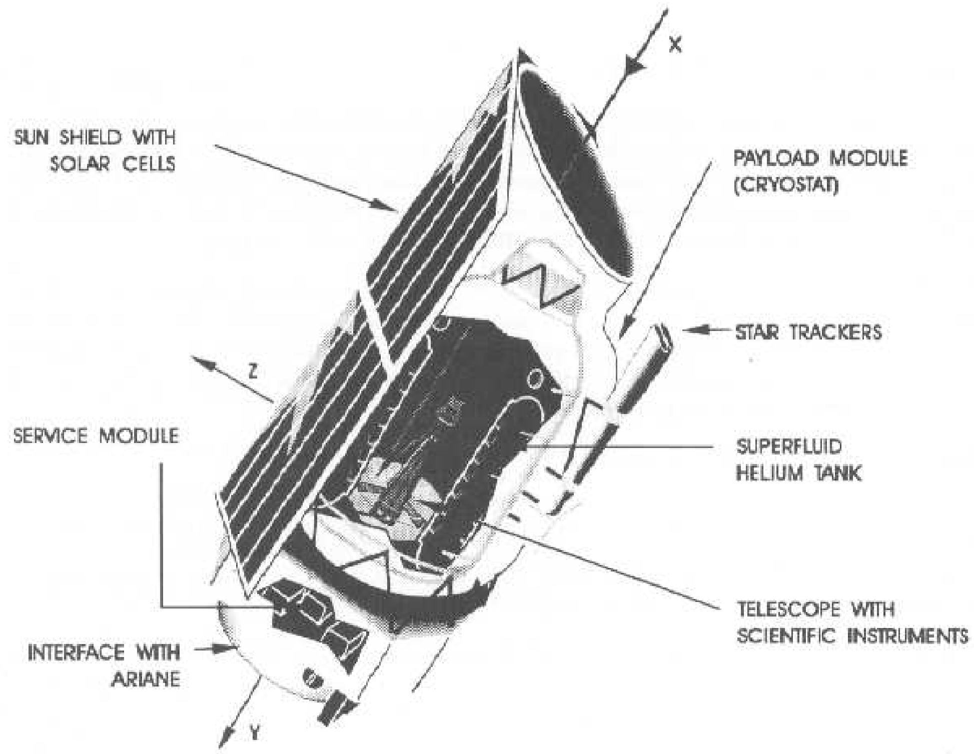

Figure C.1: The ISO spacecraft

sky, switching an instrument required a repointing of the satellite. Thus, the satellite lifetime was also limited by the amount of the remaining fuel.

C.2 Orbit

Parameters of ISO orbit are very important for observation restrictions due to celestial sources. ISO was operated in a highly–elliptical orbit with a perigee at 1000 km, an apogee at 70 000 km and a period of 24 hours. The lower parts of the orbit were inside the van Allen belts and inside these regions the scientific instruments were unusable due to effects caused by radiation impacts. ISO spent about 16 hours per day outside the radiation belt and during this time all detectors were operated. There was no on–board data storage and for scientific use ISO needs to be in continuous contact with a ground station.

ISO was not able to observe close to the Sun and strong infrared sources. The restrictions are:

1. the Sun restriction — to prevent Sun from shining to the cryostat, ISO can point only in a direction between 60 and 120 degrees away from the Sun
2. the Earth restriction — no targets closer than 77 degrees to the Earth limb were allowed
3. the Moon restriction — no targets closer than 24 degrees to the Moon were allowed
4. the Jupiter restriction — Jupiter had be kept away from the optical axis by at least 7 degrees

Due to the Earth restriction and very slow precession of the orbit ISO was not able to observe in the direction of apogee. That region is called "hole".

C.3 ISOphotometer — ISOPHOT

ISOPHOT (PHT) is the imaging photo–polarimeter on–board the Infrared Space Observatory ISO. The wavelength range that was covered by IRAS is extended by a factor of two towards longer wavelengths. This wavelength regime, which is dominated by the emission of very cool objects (15–30 K), is not accessible from the ground and only with considerably less sensitivity with airborne instruments. Since ISO was a satellite observatory designed for pointed observations, objects significantly fainter (by a factor of 100) than the IRAS survey detection limit could be measured with ISOPHOT.

ISOPHOT is composed of 3 subsystems, or sub–instruments, optimized for specific photometric modes. Only one sub–instrument can be used at a time. The sub–instruments are:

PHT–P a multiband, multi–aperture photometer with three single detectors covering wavelength range 3 – 120 μm from the near–infrared (NIR) to the far–infrared (FIR).

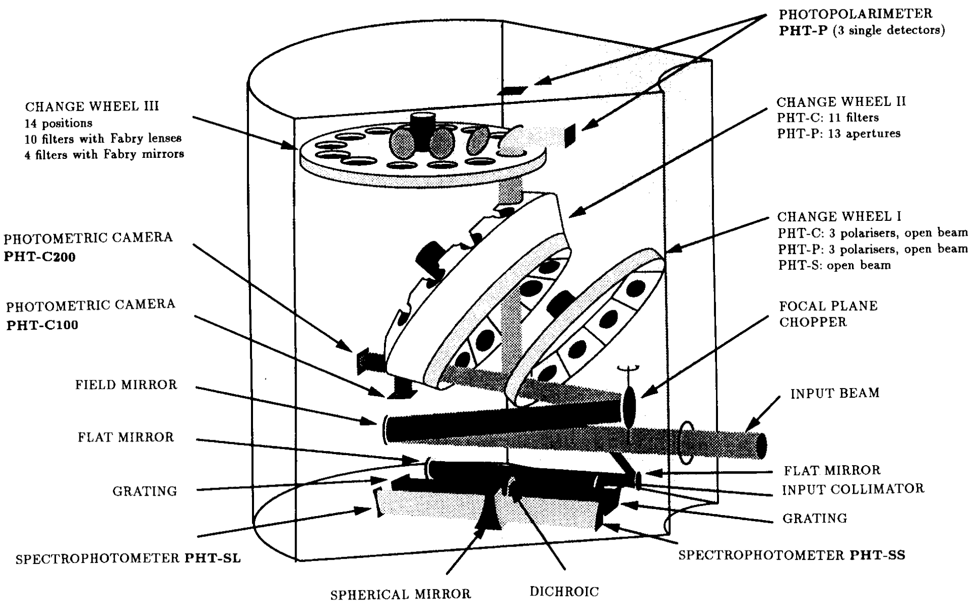

Figure C.2: Schematic view of the ISOPHOT instrument

PHT–C two photometric far–infrared (FIR) cameras for the wavelength range 50 – 240 μm.

PHT–S two grating spectrophotometers, operated simultaneously, for the wavelength ranges of about 2.5 – 5 μm and 6 – 12 μm.

The schematic view of the PHT instrument is shown on Fig. C.2. After passing the field mirror and the focal plane chopper the light beam coming from the telescope reaches change wheel I, which allows for the choice of one of the various sub–instruments and the polarimetric observing mode. The dual channel design of the PHT–S sub–instrument is indicated in the lower part of the drawing showing the dichroic element and the two PHT–S detector arrays. Both PHT–C detectors are illuminated via change wheel II, which contains the filters for theses sub–instruments. This wheel also carries the apertures for the PHT–P photometers. Finally, change wheel III contains the filters for the PHT–P sub–instruments. The fine calibration sources and the third PHT–P detector have been omitted for clarity.

Appendix D

List of program COMETBOX

The program COMETBOX was written in FWEB system[1]. FWEB is a Fortran (and also C, C++) version of Donald E. Knuth's WEB which was originally designed for Pascal. Knuth developed WEB as an environment for "Literate Programming". The fundamental logic of the WEB system encourages "top–down" programming and "structured" design. It gave me the ability to break up my work into parts called modules and allowed to have Fortran source and TEX documentation in one file `.web`. WEB contains two important program tools for `.web` file processing — tangle and weave. Tangle and weave produce `.for` and `.tex` files respectively. By this way following COMETBOX documentation was created. Because it is a separate appendix it includes another table of contents and has different page numbering.

WEB was created many year ago in times when no Object Oriented Programming and visual workbenches (Borland Pascal, Microsoft Fortran etc.) exist. Also WEB has no connections with World Wide Web.

[1]For further explanation of FWEB see (Krommes 1993).

Bibliography

[1] A'Hearn M. F., Schleicher D. G., Feldman P. D., Millis R. L. and Thompson D. T. 1984: Comet Bowell 1980b, AJ 89, p. 579–591

[2] Borovička J. 1993: A fireball spectrum analysis, A&A 279, p. 627–645

[3] Borovička J. 1994: Two components in meteor spectrum, Planet. Space Sci., Vol. 42, No. 2, p. 145–150

[4] Borovička J. and Boček J. 1995: Television spectra of meteors, Earth, Moon, and Planets 71, p. 237–244

[5] Borovička J. 1997: The spectral calibration in various orders, private communication

[6] Bradley J. P., Humecki H. J., Germani M. S. 1992: Combined infrared and analytical electron microscope studies of interplanetary dust particles, ApJ 394, p. 643–651

[7] Bregman J. D., Campins H., Witteborn F. C., Woods D. H., Rank D. M., Allamandola L. J., Cohen M. and Tielens A. G. G. M. 1987: Airborne and groundbased spectrophotometry of comet P/Halley from 5–13 micrometers, A&A 187, p. 616–620

[8] Brown P., Rendtel J., and Molau S. 1996: The outburst of the α Monocerotid meteors on 22^{nd} November 1995, ACM 96, Versailles

[9] Brownlee D. E. 1978: Microparticle Studies by Sampling Techniques, Cosmic Dust, ed. J. A. M. McDonnell, John Wiley, New York, p. 295–336

[10] Ceplecha Z., Borovička J. 1991: Meteors, in *Interrelations between physics and dynamics for minor bodies in the solar system, Benest D., Froeschle C., eds., Goutelas 1991*, p. 309–367

[11] Crovisier J., Leech K., Bockelee–Morvan D., Brooke T. Y., Hanner M. S., Altieri B., Keller H. U. and Lellouch E. 1997, Science 297, p. 1904–1907

[12] de Almeida A. A. 1996: Photoelectric photometry of comet Kohoutek (1973 XII = C/1973 E1): the production rates of CN, C_2, and solid refractory particles typical of dynamically new comets, P&SS 44, No. 4, p. 295–304

[13] Grün E., Hanner M. S., Peschke S. B., Böhnhardt H., Brooke T. Y., Campins H., Crovisier J., Heinrichsen I., Keller H. U., Knacke R., Krüger H., Lamy P., Leiner Ch., Lemke D., Lisse C. M., Müller M., Osip D. J., Šolc M., Stickel M., Sykes M., Vanýsek V., Zarnecki J. 1998: Broadband Infrared Photometry of Comet Hale–Bopp with ISOPHOT, A&A, in preparation

[14] Hallenbeck S. L., Nuth J. A. III, Daukantas P. L. 1998: Mid–Infrared Spectral Evolution of Amorphous Magnesium Silicate Smokes Annealed in Vacuum: Comparison to Cometary Spectra, Icarus 131, p. 198–209

[15] Hanner M. S. 1981: Effect of the Size Distribution on the Thermal Emission From Cometary Dust, Cometary Science Team Preprint Series, Jet Propulsion Laboratory, No. 23

[16] Hanner M. S., Newburn R. L., Gehrz R. D., Harrison T. and Ney E. P. 1990: The infrared spectrum of comet Bradfield (1987s) and the silicate emission feature, ApJ 348, p. 312–321

[17] Hanner M. S., Hackwell J. A., Russell R. W., and Lynch D. K. 1994: Silicate Emission Feature in the Spectrum of Comet Mueller 1993a, Icarus 112, p. 490–495

[18] Hanner M. S., Lynch D. K., Russell R. W., Hackwell J. A., Kellogg R. 1996: Mid–Infrared Spectra of Comets P/Borrelly, P/Faye, and P/Schaumasse, Icarus 124, p. 344–351

[19] Hanner M. S., Veeder G. J., Tokunaga A. T. 1992: The dust coma of comet P/Giacobini–Zinner in the infrared, AJ 104, p. 386–393

[20] Hanner M. S., Gehrz R. D., Harker D. E., Hayward T. L., Lynch D. K., Mason C. C., Russell R. W., Williams D. M., Wooden D. H., and Woodward C. E. 1998: Thermal emission from the dust coma of comet Hale–Bopp and the composition of the silicate grains, Earth, Moon, and Planets, in press

[21] Hemenway C. L., Swider A., and Bowman C. 1971: Meteor spectroscopy using an image orthicon, Canadian Journal of Physics 49, p. 1361–1394

[22] Huffman, D. R. and Stapp J. L. 1973: in Interstellar Dust and Related Topics, ed. J. M. Greenberg and H. C. van de Hulst, p. 297–301

[23] Huffman, D. R. 1977: Interstellar Grains. The Interaction of Light with a Small-particle System, Advances in Physics, Vol. 26, p. 129–230

[24] Jenniskens P., de Lignie M. and Betlem H. 1996: A meteor storm provided the first observations of the IRAS dust trail in the orbit of a long period comet, ACM 96, Versailles

[25] ISO Info No. 13 – May 1998,
`http://www.iso.vilspa.esa.es/isoinfo/isoinfo-13/`

[26] Jenniskens P., Betlem H., de Lignie M., and Langbroek M. 1997: The detection of a dust trail in the orbit of an Earth–threatening long–period comet, ApJ 479, p. 441–447

[27] Jenniskens P. and Docters van Leeuwen G. 1997a: The α–Monocerotids meteor outburst: the cross section of a comet dust trail, Planet. Space Sci., Vol. 45, No. 12, p. 1649–1652

[28] Jewitt D. and Luu J. 1992: Submillimeter Continuum Emission from Comets, Icarus 100, p. 187–196

[29] Koike C. and Shibai H. 1990: Optical constants of hydrous silicates from 7 to 400 μm, Mon. Nat. R. Astron. Soc. 246, p. 332–336

[30] Koike C. and Tsuchiyama A. 1992: Simulation and alteration for amorphous silicates with very broad bands in infrared spectra, Mon. Not. R. Astron. Soc. 255, p. 248–254

[31] Koike C., Shibai H. and Tuchiyama A. 1993: Extinction of olivine and pyroxene in the mid– and far–infrared, Mon. Not. R. Astron. Soc. 264, p. 654–658

[32] Krommes J. A. 1993: FWEB User Manual, `ftp://ftp.pppl.gov/pub/fweb/`

[33] Kruchinenko V. G., Kazantsev A. M., Taranukha Yu. G., Kozak P. M., Yeryomin S. S., Rozhilo O. O., Smertyuk L. M. 1997: Catalogue of Perseid shower meteor on TV observation in Kyiv during 1991–1993, Visnik Kyivskogo universitetu, Astronomiya, V. 34, p. 94–117

[34] Massone L. et al. 1985: ACM II, p. 410

[35] Massone L. 1987: PhD Thesis

[36] Millman P. M., Cook A. F., and Hemenway C. L. 1971: Spectroscopy of Perseid meteors with an image orthicon, Canadian Journal of Physics 49, p. 1365–1373

[37] Millman P. M. and Clifton K. S. 1975: SEC Vidicon spectra of Geminid meteors, 1972, Canadian Journal of Physics 53, p. 1939–1947

[38] Millman P. M. and Clifton K. S. 1979: Video techniques in comet–debris studies, Sky & Telescope, Vol. 57, No. 1

[39] Mukhamednazarov S. and Maltseva N. V. 1989: Study of the TV spectrograms of meteors, Astron. Vestnik 23, p. 297–303; Sol. Syst. Res. 23, p. 179–183

[40] Oberst J., Molau S., Heinlein D., Gritzner C., Schindler M., Spurný P., Ceplecha Z., Rendtel J. and Betlem H. 1998: The "European Fireball Network": Current status and future prospects, Meteoritics & Planetary Science, Vol. 33, p. 49–56

[41] Padevět V. and Boček J. 1992: Television observation of meteors, Meteoroids and their parent bodies, Smolenica

[42] Padevět V. and Jakeš P. 1993: Comets and meteorites: relationship (again?), A&A 274, p. 944–954

[43] Richter K. and Keller H. U. 1995: On the Stability of Dust Particle Orbits around Cometary Nuclei, Icarus 114, p. 355–371

[44] Sandford S. A. and Walker R. M. 1985: Laboratory infrared transmission spectra of individual interplanetary dust particles from 2.5 to 25 microns, ApJ 291, p. 838–851

[45] Spurný P. 1991: Odvození vlastností meteorického roje Geminid z fotografických záznamů, PhD Thesis, Ondřejov

[46] Storrs A. D., Cochran A. L. and Barker E. S. 1992: Spectrophotometry of the Continuum in 18 comets, Icarus 98, p. 163–178

[47] Štork R. 1993: Porovnání chemického složení kometárního prachu a meteorů, Master Thesis, Charles University Prague

[48] Štork R. and Šolc M. 1996: Models of dust temperatures in atmospheres of ISO target comets, Meteoritics & Planetary Science 31, No. 4 Supp., p. A135

[49] Štork R., Borovička J., Boček J. and Šolc M. 1998: Peculiar features of α Monocerotid television spectra, Meteoritics & Planetary Science 33, No. 4 Supp., p. A151

[50] Wooden D. H., Harker D. E., Woodward C. E., Butner H. M., Koike C., Witteborn F. C., McMurtry C. M. 1998: Silicate mineralogy of the dust in the inner coma of comet C/1995 O1 (Hale–Bopp) pre– and post–perihelion, ApJ, in press

[51] ESA 1994: ISO Observer's Manual, ESA/ESTEC, Noordwijk, the Netherlands

[52] ESA 1994: ISOPHOT Observer's Manual, ESA/ESTEC, Noordwijk, the Netherlands

[53] ESA 1994: Guaranteed Time Programme Part A–C, ESA/ESTEC, Noordwijk, the Netherlands